Advanced Energy Materials

ADVANCED ENERGY MATERIALS
www.advenergymat.de

RESEARCH ARTICLE

Attaining the Sabatier Sweet Spot via d-Orbital Occupancy Engineering for High-Performance Zn–Air Batteries

Srijib Das[1,2] | Arupjyoti Pathak[3] | Sk. Mukaddar[3] | Rajashri R. Urkude[4] | Tapas Kuila[1,2] | Ranjit Thapa[3,5] | Aniruddha Kundu[6]

[1]Electric Mobility & Tribology Research Group, CSIR- Central Mechanical Engineering Research Institute, Durgapur, India | [2]Academy of Scientific and Innovative Research (AcSIR), Ghaziabad, India | [3]Department of Physics, SRM University – AP, Amaravati, Andhra Pradesh, India | [4]Beamline Development & Application Section, Bhabha Atomic Research Center Trombay, Mumbai, India | [5]Centre for Computational and Integrative Sciences, SRM University -AP, Amaravati, Andhra Pradesh, India | [6]Centre for Interdisciplinary Research, SRM University-AP, Amaravati, Andhra Pradesh, India

Correspondence: Tapas Kuila (tkuila.cmeri@csir.res.in) | Ranjit Thapa (ranjit.t@srmap.edu.in) | Aniruddha Kundu (aniruddha.k@srmap.edu.in)

Received: 15 November 2025 | **Revised:** 23 March 2026 | **Accepted:** 27 March 2026

Keywords: d-orbital occupancy | gel-electrolyte | interface engineering | oxygen electrocatalysis | Zn–air battery

ABSTRACT

Precise control of oxygen-intermediate binding near the Sabatier optimum is crucial for designing high-performance oxygen electrocatalysts for zinc–air batteries (ZABs). In CoFe bimetallic alloys, Co nanoclusters predominantly drive the oxygen evolution reaction (OER), while Fe sites promote the oxygen reduction reaction (ORR), albeit with kinetic limitations. Achieving superior oxygen activity thus demands rational modulation of d-orbital occupancy via engineered heterointerfaces. Herein, we report a dual N-source-assisted partial nitridation strategy that in situ forms Co_4N adjacent to the CoFe alloy (CNFC-3), resulting in a well-defined heterointerfacial interface within N-doped graphitic carbon tubes. Combined experimental and theoretical analyses reveal that orbital coupling between nitride and alloy species optimizes oxygen intermediate adsorption, expediting *OH formation for ORR and *OOH formation for OER. This synergy results in an ultra-low oxygen overpotential ($\Delta E \approx 0.631$ V) and nearly 4-electron selectivity. Notably, CNFC-3-based liquid ZABs deliver a high-power density of ≈201 mW cm^{-2} and a specific capacity of 812 mAh g_{Zn}^{-1}. At larger scales, ZABs incorporating the same catalyst also demonstrate promising performance. Furthermore, flexible ZABs employing NTA-modified P-P-N gel exhibit temperature resilience, dendrite suppression, and robust durability under high current densities, indicating their potential for next-generation alternative batteries.

1 | Introduction

The growing demand for flexible and foldable electronics necessitates the development of safe, high-energy, and sustainable rechargeable batteries that surpass the limitations of current technologies. According to the US Department of Energy, next-generation energy storage systems must deliver an energy density of more than 300 Wh kg^{-1}, operate reliably over a wide temperature range, and remain cost-effective with a long cycle life and high safety [1, 2]. Among various alternatives, aqueous zinc–air batteries (ZAB) and quasi-solid-state-flexible zinc–air batteries (QSSFZBs) offer compelling advantages, including high theoretical energy density, intrinsic safety, and mechanical adaptability [3, 4]. Yet, practical realization is still hindered due to sluggish bifunctional O_2 redox kinetics, lack of robust cathode materials, and limited electrolyte compatibility across diverse temperatures [5, 6]. To overcome these challenges, the design of dual-active-site air-cathodes coupled with quasi-solid-state-gel electrolytes

Srijib Das and Arupjyoti Pathak contributed equally to this study.

is crucial for achieving high performance across wide operating conditions [7, 8]. Noble metal-based catalysts such as RuO_2 and Pt/C can effectively decrease O_2 redox reaction overpotential, but suffer from high cost and poor durability, limiting scalability. Despite notable progress, only a limited number of materials exhibit high bifunctional catalytic activity. The pursuit of such bifunctional electrocatalysts is particularly appealing, as they offer the potential to streamline fabrication processes, reduce material diversity, and significantly lower overall production costs.

Recently, bimetallic alloys have gained attention as electrocatalysts due to synergistic electronic interactions that promote charge redistribution and reduce reaction energy barriers. For example, it is demonstrated that host–guest engineered CoFe alloy-embedded bimetallic MOF-derived carbon nanocomposites deliver a half-wave potential ($E_{1/2}$) of 0.89 V with outstanding stability over 30,000 cycles for ORR [9]. Similarly, FeCo nanoparticles encapsulated in graphitic carbon along with Co_2P anchored on N, P-co-doped carbon nanofibers (FeCo/Co_2P@NPCF) was designed which achieve a reduced ΔE of 0.77 V and enabling ZAB with a power density of 154 mW cm^{-2} and a charge–discharge gap of 0.83 V [10]. Furthermore, Liu et al. developed a hybrid FeCo-TA@CMS catalyst using melamine sponge and bimetal-polyphenol network comprising FeCo alloy nanoparticles embedded in porous N-doped carbon, which achieved a $E_{1/2}$ of 0.83 V, superior durability under harsh conditions, and an OER overpotential of 0.38 V at 10 mA cm^{-2} [11]. A hierarchical CoFe@NC-NT architecture consisting of N-doped carbon nanotubes armored with carbon-layer-capped CoFe alloy was synthesized, which exhibits an OER overpotential of 0.257 V and ORR $E_{1/2}$ of 0.74 V; the enhanced activity and stability were attributed to efficient electronic contact between conductive nanotubes and alloy nanoparticles and protective carbon encapsulation [12]. Kim et al. demonstrated that strongly coupled FeCo alloy nanoparticles on defect-rich N-doped carbon exhibit enhanced bifunctional activity, achieving a $E_{1/2}$ of 0.892 for ORR and an overpotential of 0.362 V at 10 mA cm^{-2} for OER [13]. Apart from that, the transition metal nitrides (TMNs) are widely explored in electrocatalysis owing to their low cost and simultaneous presence of abundant M—N covalent and M—M metal bonds [14]. The incorporation of N atoms in the transition metals facilitates expanding the lattice spacing and hence, the density of states near the Fermi level is increased [15]. As a consequence, formation of OER intermediates is promoted, and at the same time, the adsorption energies of reaction intermediates at the catalyst surface can be adjusted. Among the TMNs, cobalt nitrides like Co_4N have emerged as promising alternatives due to their metallic conductivity and favorable OER activity [16, 17]. However, their ORR performance remains suboptimal, primarily due to weak electron donation and inefficient hydroxyl formation [18, 19]. Significant research progress has been made in designing Co_4N for improved oxygen electrocatalysis. The most common method involves pyrolysis of metal-organic frameworks (MOFs) or covalent organic frameworks (COFs), resulting in Co_4N nanoparticles supported on carbon substrate [20–23]. However, this approach is constrained by complex synthesis protocols and a limited selection of precursors. Alternative strategies employing metal salts and nitrogen-rich organic compounds have emerged, yet these often require corrosive NH_3 gas for nitridation or involve multi-step procedures that hinder scalability [24–28]. To harness inherent OER performance of Co_4N alongside its promising ORR performance, tuning the d-band center via incorporation of a secondary transition metal presents a compelling strategy. Theoretically, introducing elements such as Fe or Co can downshift the d-band relative to the Fermi level, facilitating desorption of oxygenated intermediates. Nonetheless, achieving simultaneous incorporation and synergistic interaction remains challenging due to disparate synthetic conditions and structural complexity [29–31]. Two key questions persist: (i) How can the accessibility and utilization of active sites be maximized? (ii) What role does the local electronic environment play in modulating catalytic activity?

As shown in Figure 1a, a systematic structural comparison was undertaken to rationally design a robust and efficient bifunctional electrocatalyst. Monometallic counterparts, such as Co@NC, Fe@NC, and Co_4N@NC, serve as foundational models but suffer from limited electronic tunability and imbalanced ORR/OER activity due to fixed d-orbital configurations. While CoFe alloys enhance charge conductivity, they lack interfacial modulation of active sites. Without heterointerfacial Co_4N/CoFe systems, partial electronic coupling is introduced, yet spatial separation limits synergistic effects. To overcome these limitations, a heterointerfacial Co_4N/CoFe@NC configuration is constructed, wherein intimate interfacial sites enable strong orbital hybridization, rapid charge redistribution, optimal antibonding orbital occupancy, and favorable d-band center alignment. This design, guided by theoretical screening and electronic structure calculations, demonstrates how heterointerfacial coupling enhances bifunctional performance by improving interfacial charge transfer and regulating intermediate binding. Building on these insights, we developed a scalable, cost-effective strategy to fabricate a dual-active-site catalyst, namely CNFC-3, anchored to a nitrogen-doped graphitic carbon matrix. This composite architecture is expected to provide abundant exposed active sites, enhanced charge transfer, and improved structural stability during electrochemical operation. Through detailed analysis of electronic structure and comprehensive screening, we identified key descriptors that govern the catalytic performance. Notably, CNFC-3 exhibits a d-band center (ε_d) positioned closer to the Fermi level, and a high d-band occupancy (O_d) up to the Fermi level, suggesting enhanced orbital overlap with oxygen intermediates. This electronic configuration minimizes the occupancy of antibonding states, promoting optimal bonding and efficient electron transfer. Can such a dual-phase architecture serve as a next-generation bifunctional catalyst for energy devices? Can this approach bridge the gap between theoretical design and practical application? These findings offer valuable insights into the structure–activity relationship and suggest new directions for the development of advanced electrocatalysts. The as-designed CNFC-3 catalyst exhibited excellent oxygen redox reversibility with a small potential gap of ≈0.631 V. CNFC-3-based aqueous ZAB exhibited a specific capacity of 812 mAh g_{Zn}^{-1} and power density of ≈201 mW cm^{-2}. Furthermore, the CNFC-3-based air electrode exhibited a remarkable ampere-hour-level discharge capacity. The quasi-solid-state, flexible ZABs based on CNFC-3 exhibit robust operation over a wide temperature range, underscoring their practical applicability. This study presents a strategy for optimizing CNFC-based catalysts via d-orbital modulation, offering new insights into bifunctional catalysis and guiding the development of next-generation energy conversion materials.

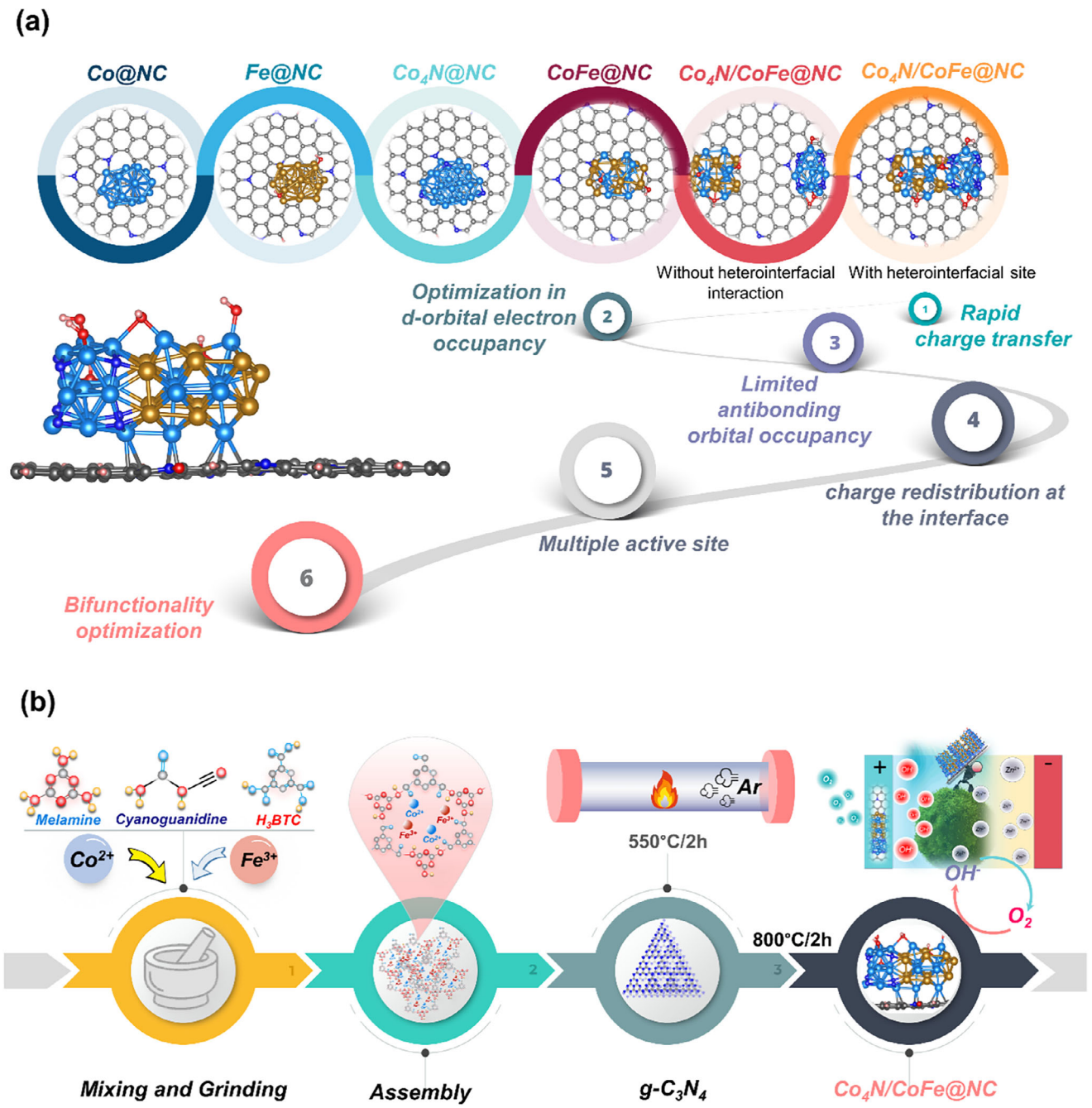

FIGURE 1 | (a) Schematic representation of different electrocatalyst configurations: Co@NC, Fe@NC, Co_4N@NC, CoFe@NC, Co_4N/CoFe@NC (without heterointerfacial site), and Co_4N/CoFe@NC (with heterointerfacial site), highlighting the progressive structural evolution and its impact on electronic interaction, active site synergy, and catalytic efficiency toward oxygen electrocatalysis (ORR/OER). (b) Schematic illustration for the synthesis procedure of the electrocatalyst.

2 | Results and Discussion

2.1 | Synthesis and Physicochemical Characterizations

The synthesis of Co_4N/CoFe@NC was achieved through a facile two-step process, as illustrated in Figure 1b. Initially, a mechanochemical approach was used to grind the nitrogen and carbon precursors in the presence of metal salts (Fe and Co), and subsequently, a two-step pyrolysis process was performed under an Ar atmosphere at different temperatures (Supporting Information for the detailed experimental procedure). During the pyrolysis process, the metal ions were transformed into metal nanoalloy, and metal nitride was decorated on the carbon sheet along with the formation of carbon tubes at higher temperatures. This occurred due to the in situ generation of NH_3 gas (Video S1). Herein, to understand the formation of metal nanoalloys and transition metal nitrides, we have varied the molar ratio of metal salts. For this purpose, three different sets of catalysts denoted as Co_4N/Co_1Fe_2@NC (CNFC-1), Co_4N/CoFe@NC (CNFC-2), and Co_4N/Co_2Fe_1@NC (CNFC-3), respectively, were synthesized at 800°C. To check the effect of pyrolysis temperature,

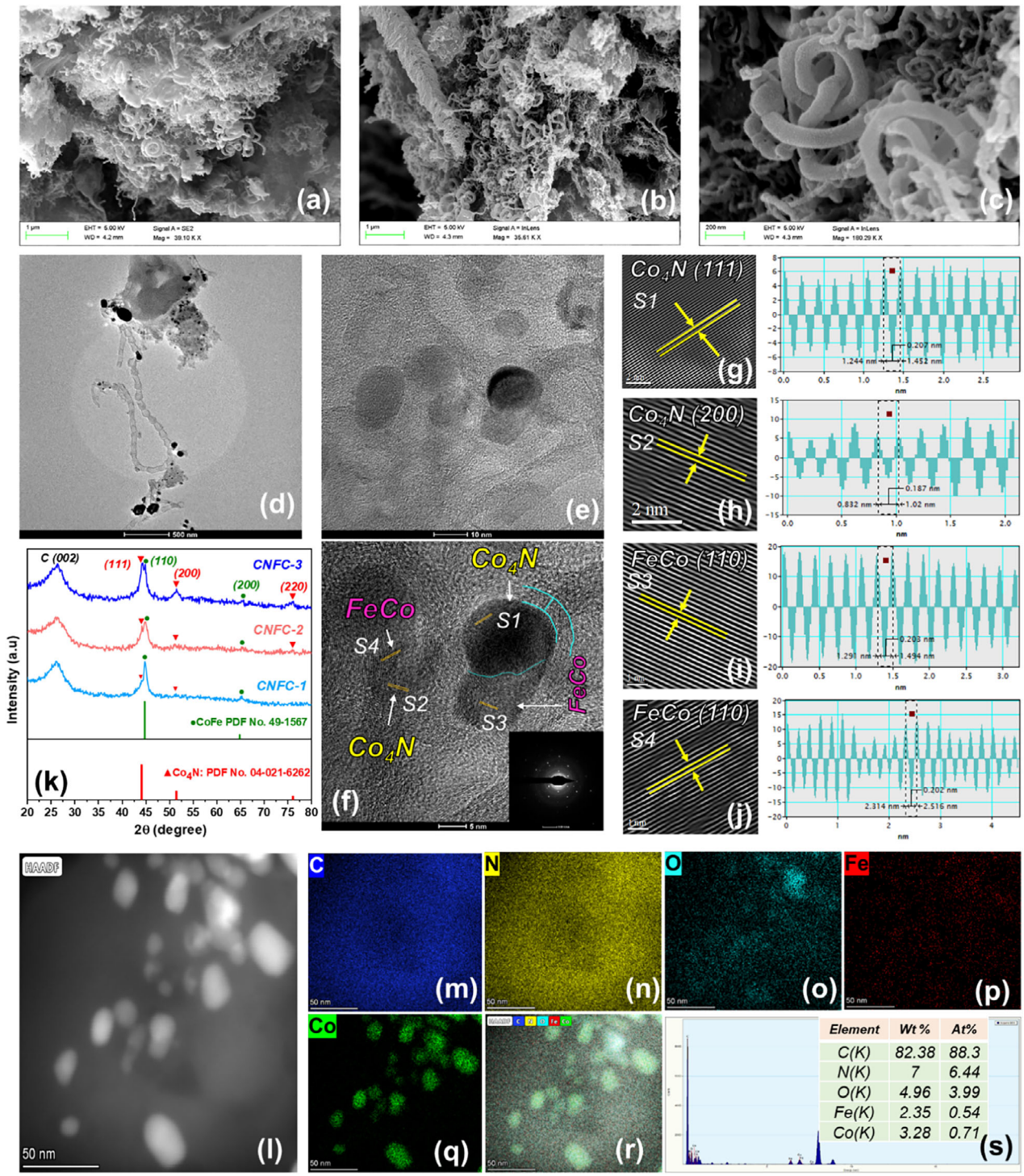

FIGURE 2 | (a–c) FE-SEM images of CNFC-3 at different magnifications, (d–f) TEM and HR-TEM images of CNFC-3, (g–j) IFFT pattern of the selected region and corresponding line spectrum showing the d-spacing of the lattice, (k) PXRD pattern of CNFC-1, CNFC-2, and CNFC-3 with standard XRD pattern. (l) HAADF- STEM image of CNFC-3, and corresponding elemental mapping (m–r), (s) EDX spectrum of CNFC-3.

CNFC-3 was also synthesized at 700°C and 900°C. Additionally, to investigate the synergistic effect of the dual phase, monometallic counterparts Co_4N-NC (CN-NC) and Fe-NC (Fe-NC) were also synthesized and will be discussed later.

The synthesized electrocatalysts were systematically characterized using different microscopic and spectroscopic techniques. Field-emission scanning electron microscopy (FE-SEM) was employed to probe the surface morphology and microstructure of the catalysts. The representative FE-SEM images (Figure 2a–c and Figure S1) reveal that the designed CNFC-3 catalyst features evenly decorated carbon tubes and porous carbon sheets. Energy-dispersive spectrum (EDS) and corresponding EDS elemental mapping images confirm the homogeneous distribution of Fe, Co, C, N, and O elements (Figure S1). However, the same catalyst synthesized at a pyrolysis temperature of 700°C, predominantly

exhibits a sheet-like architecture, whereas CNFC-900 (CNFC-3 synthesized at 900°C) is dominated by relatively shorter graphitic carbon tubes than CNFC-3 (Figure S2). In contrast, CNFC-2 displays crumpled carbon sheets embedded within a porous network (Figure S3a,b), while CNFC-1 exhibits tubular nanostructures accompanied by aggregated carbon sheets (Figure S3c,d). The EDS spectrum and EDS elemental mappings for these two catalysts are provided in Figures S4 and S5. The abundance of elongated and interconnected tubular networks and the presence of porous carbon domains in CNFC-3 are expected to accelerate surface redox kinetics by facilitating efficient charge transfer and mass transport. However, to precisely characterize the catalyst morphology, high-resolution transmission electron microscopy (HR-TEM) was performed. The TEM images of the CNFC-3 catalyst (Figure 2d,e) show abundant heterointerfacial sites between Co_4N and CoFe nanoparticles, which are anchored on both carbon sheets and tubes and extend several micrometers in length. The HR-TEM image and the corresponding inverse fast Fourier transform (IFFT) images provide detailed structural visualization, confirming the nanoscale dispersion and crystallinity of the active sites [Figure 2f–j and Figure S6a (enlarged view)]. The calculated lattice spacing of 0.207 and 0.187 nm is consistent with the (111) and (200) crystal planes of a face-centered cubic (fcc) Co_4N phase (Figure 2g,h), while the spacing of 0.203 nm is attributed to the (110) plane of the alloyed CoFe phase (Figure 2i,j). The slightly expanded (111) lattice spacing in Co_4N relative to metallic Co is likely due to nitrogen incorporation during nitridation, which induces local distortions without altering the overall crystal symmetry [30, 31]. Selected area electron diffraction (SAED) further validates the polycrystalline nature of CNFC-3 (Figure 2f, inset). Notably, CoFe alloy nanoparticles are encapsulated by carbon shells with an interlayer spacing of 0.34 nm, consistent with the (002) plane of graphitic carbon (Figure 2f and Figure S6b,c).

Powder X-ray diffraction (XRD) analysis corroborates the crystallographic assignments. CNFC-3 exhibits dominant reflections at 44.3°, 51.5°, and 76.1°, indexed to the (111), (200), and (220) crystalline facets of cubic Co_4N (PDF No: 04-021-6262; Figure 2k). These findings align well with the HR-TEM-derived d-spacings, confirming the formation of single-phase cobalt nitride rather than metallic Co. Additional peaks centered at 44.9 and 65.6° are assigned to the (110) and (200) crystalline facets of body-centered cubic (*bcc*) bimetallic CoFe alloys (PDF No: 49–1567). Interestingly, increasing the Fe precursor ratio (Fe:Co = 2:1 or 1:1) suppresses nitride formation and promotes the emergence of an alloy phase, underscoring the critical role of metal ion ratios in directing phase evolution toward either nitrides or bimetallic alloys. Thus, PXRD analysis confirms the simultaneous formation of multiple active phases, including Co_4N nanoparticles and CoFe alloys, within the CNFC-3 catalyst. The presence of these phases is expected to play a pivotal role in enhancing electrocatalytic performance. Additionally, a sharp diffraction peak at $2\theta \approx 26.2°$, observed across all synthesized catalysts, corresponds to the (002) planes of graphitic carbon. The XRD patterns of CNFC-3 synthesized at different temperatures are shown in Figure S7, which clearly indicate that the pyrolysis temperature plays a vital role in determining the alloy/nitride phase. For comparison, the use of Co-salt alone led to the exclusive formation of the Co_4N phase, as evidenced from the PXRD pattern in Figure S8a. In contrast, using only the iron precursor yielded Fe-NC (Figure S8b) with a characteristic diffraction peak at ≈44.6°, corresponding to metallic Fe embedded within the carbon matrix. The TEM images for CNFC-1 and CNFC-2 (Figures S9 and S10) reveal a progressive decline in the formation of heterointerfacial sites between Co_4N and FeCo alloy phases with decreasing Co content, a trend particularly pronounced from CNFC-2 to CNFC-1. High-angle annular dark-field scanning transmission electron microscopy (HAADF-STEM) image, corresponding elemental mapping, and EDX spectra of CNFC-3 further confirm the uniform spatial distribution of the constituent elements (Figure 2l–s). Moreover, to examine the spatial distribution of Fe and Co within the different clustered domains, high-resolution aberration-corrected HAADF-STEM (AC-HAADF-STEM) and electron energy-loss spectroscopy (EELS) analyses were performed (Figure S11). These results clearly demonstrate the coexistence of Fe and Co within nanoscale clusters, with both elements uniformly distributed across the nanoclusters in different regions (Figure S11A,B). These findings further confirm the formation of Co/Fe-based nanostructures and establish the presence of abundant heterointerfaces between the metallic/nitride nanoparticles and the surrounding N-doped carbon matrix. To further check the formation of atomically dispersed M-Nx species, AC-HAADF-STEM analysis was performed. The AC-HAADF-STEM images acquired from the thin carbon support regions reveal isolated bright spots, which are characteristic of atomically dispersed metal species. Corresponding EELS elemental mapping further confirms the distribution of Fe and Co at the atomic level within the N-doped carbon matrix, supporting the presence of single-atom M-Nx configurations (Figure S12).

Collectively, these results indicate a hierarchical catalyst architecture comprising atomically dispersed M-N_x sites and CoFe/Co_4N nanoclusters, wherein the abundant heterointerfaces are expected to facilitate electronic coupling and synergistic catalytic activity. The SAED and HAADF-STEM images of CNFC-1 and CNFC-2, as shown in Figures S13–S16, corroborate the polycrystalline nature and homogeneous dispersion of the active components.

The influence of pyrolysis temperature on the specific surface areas and pore size distributions of CNFC-3, synthesized at different temperatures, was evaluated via N_2 adsorption–desorption measurements at 77.35 K. All samples exhibit typical type-IV isotherms with pronounced hysteresis loops (Figure S17a), confirming mesoporous characteristics. CNFC-3 synthesized at 800°C displays the highest specific surface area (218.25 $m^2\ g^{-1}$), exceeding those of synthesized at 700°C (125.82 $m^2\ g^{-1}$) and 900°C (177.15 $m^2\ g^{-1}$). Moreover, BJH desorption analysis (Figure S17b–d) further reveals comparable pore volumes for CNFC-700, CNFC-800, and CNFC-900, respectively, with a mode pore diameter of ≈3.63 nm. Furthermore, ICP-OES quantified the Co and Fe contents in the CNFC-3 catalyst at 8.61 and 3.42 wt%, respectively, corresponding to a Fe:Co ratio of ≈1:2.5.

X-ray photoelectron spectroscopy (XPS) was employed to investigate the bonding configurations and chemical states of the catalysts. The survey spectra confirm (Figure S18) the presence of the desired constituent elements C, N, O, Fe, and Co. As shown in the high-resolution Co 2p spectrum (Figure 3a, Table S1), the deconvoluted peaks can be assigned to metallic Co—Co

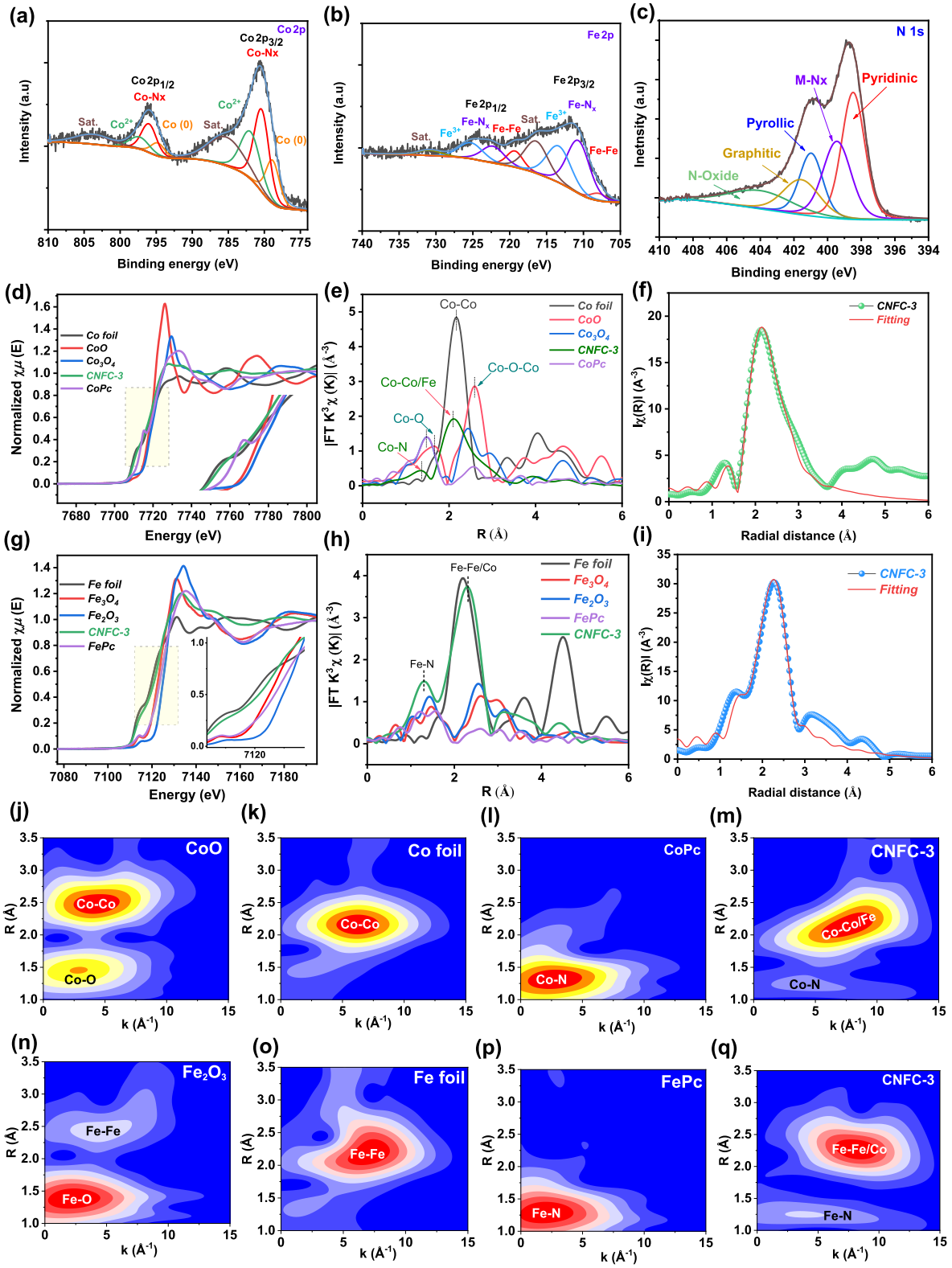

FIGURE 3 | Deconvoluted high-resolution XPS spectra of (a) Co 2p, (b) Fe 2p, (c) N 1s, normalized XANES spectra of (d) CNFC-3 Co k-edge, (e) Fourier transformed, and (f) Fitted EXAFS spectra, (g–i) corresponding XANES, Fourier transformed EXAFS, and fitted EXAFS spectra of Fe k-edge, (j–q) corresponding WT contour plots of Co and Fe of CNFC-3 with standards respectively.

bonding (Co $2p_{3/2}$ at 778.8 eV and Co $2p_{1/2}$ at 794.7 eV), Co—N_X coordination (780.4 and 795.9 eV), and Co^{2+} species (781.9 and 797.3 eV), along with a characteristic shake-up satellite located at higher binding energies (785.2 and 803.7 eV). These features concurrently indicated the coexistence of different kind of Co in Co_4N, Co—N_x and metallic Co—Co configurations [32–38].

The high-resolution Fe 2p spectrum (Figure 3b, Table S2) indicates the zero-valence state of Fe (707.9 and 719.29 eV), suggesting the metallic Fe in CoFe alloy. The two peaks at 710.7 and 722.3 eV are ascribed to Fe^{2+} state of Fe $2p_{3/2}$ and Fe $2p_{1/2}$, respectively, implying the existence of Fe—N_x species, whereas the peaks at 713.3 and 725.3 eV are assigned to Fe^{3+} state [34, 39]. The deconvoluted N 1s spectra reveal five different types of nitrogen species, pyridinic-N, M-Nx, pyrrolic-N, Graphitic-N, and N-oxide located at 398.5, 399.4, 400.9, 401.6, and 404.1 eV, respectively (Figure 3c), supporting the coexistence of Co—N and C—N/C═N species [40–43]. Notably, CNFC-3 exhibits enriched Co—N, graphitic-N, and pyridinic-N content (Figure S19), which may enhance electrocatalytic activity by increasing redox-active sites and conductivity while reducing charge-transfer resistance. High-resolution C 1s spectra (Figure S20) confirm oxygenated functionalities and effective N-doping into the carbon lattice, which may serve as an active site to improve ORR activity. The O 1s spectra identify three peaks corresponding to different oxygen species, including lattice oxygen (M—O), hydroxide (—OH), and chemisorbed water (O_w) (Figure S21), suggesting improved hydrophilicity and electrolyte interaction, which is crucial for oxygen electrocatalysis [41–44]. Moreover, to further probe the electronic coupling, XPS analysis was performed on the control CN-NC sample and compared with the CNFC-3 catalyst (Figure S22). For CN-NC, the Co $2p_{3/2}$ region exhibits a dominant peak centered at ≈778.1 eV, which is a signature of metallic Co—Co bonding environment in Co_4N, accompanied by a higher-binding-energy component at ≈780.0 and 781.6 eV assigned to Co—N_X coordination and partially oxidized Co^{2+} species at the surface. The metallic Co species (Co^0) originate from Co—Co bonding within the Co_4N lattice, which preserves the intrinsic metallic character of the framework. In contrast, the oxidized Co components are associated with Co—N coordination environments, indicating charge transfer from Co toward the more electronegative N atoms. In contrast, CNFC-3 displays a positive shift of the Co $2p_{3/2}$ region towards higher binding energy. The Co-N_X feature at Co $2p_{3/2}$ in CNFC-3 is shifted by ≈0.3 eV; a similar trend is observed for the Co^{2+}, indicating that the overall chemical state of Co is preserved but electronically modulated, further confirming that the modification affects the entire spin–orbit pair rather than isolated components. Consistent chemical environments across CNFC-1 and CNFC-2 are further validated by deconvoluted XPS spectra (Figures S23 and S24). To elucidate the electronic states and local coordination environments of Co and Fe in CNFC-3, X-ray absorption spectroscopy (XAS) was employed, complemented by reference spectra from standard compounds including elemental foils, oxides (CoO, Co_3O_4, Fe_2O_3, Fe_3O_4), and phthalocyanines (CoPc, FePc). Synchrotron-based extended X-ray absorption fine structure (EXAFS) and X-ray absorption near-edge structure (XANES) measurements at the Co and Fe K-edges provided atomistic insights into the coordination geometry and oxidation states. Co K-edge XANES (Figure 3d) spectra revealed a pre-edge feature at 7709.8 eV, characteristic of Co—N coordination, corresponding to the 1s to 3d core-level transition, consistent with cobalt nitride [45]. The main edge position (due to transition from core-level 1s to empty 4p) and intensity closely resembled that of metallic Co foil, indicating the presence of zero-valent Co species. Fourier-transformed EXAFS (FT-EXAFS) spectra in R-space displayed two prominent peaks: a dominant signal at ≈2.15 Å attributed to Co—Co interactions within a CoFe alloy framework, and a secondary peak at ≈1.39 Å (Figure 3e), distinct from Co—O or Co—Co in foil, assigned to Co—N coordination. Furthermore, to quantitatively evaluate the local coordination environment, the XAS fitting parameters is supplemented in Table S3. The Co—N coordination number is 2.1±1.2, which is significantly lower than the ideal coordination in CoPc, indicating a distorted or partially coordinated M—N environment rather than a well-defined MN_4 site. Quantitative fitting of the EXAFS data (Figure 3f and Table S3) further confirmed the coexistence of Co—Co and Co—N bonds, with Co—Co scattering dominating, indicative of alloy formation with embedded nitrogen coordination. Similarly, the XANES and FT-EXAFS for Fe K-edge are demonstrated in Figure 3g–l. Fe K-edge XANES spectra of CNFC-3 exhibited a pre-edge peak near 7114 eV (Figure 3g) and an absorption edge intermediate between Fe foil and FePc/Fe_3O_4, suggesting a mixed-valence state of Fe spanning 0 to +3. This intermediate edge position implies strong electronic coupling between Fe nanoclusters and adjacent Co sites. The positive oxidation states of both Co and Fe indicate electron delocalization toward neighboring nitrogen atoms, thereby enhancing the redox accessibility of the metal centers [46]. In the Fe K-edge FT-EXAFS spectra, a peak at ≈ 1.3–1.5 Å (Figure 3h,i), nearly identical to the Fe—N-related peak of FePc, while a second peak at ≈2.32 Å was assigned to Fe—Fe/Co interactions, confirming the dual presence of Fe—N motifs and Fe-based clusters (Table S4) [47, 48]. The Fe—N coordination number was found to be 3.0±1.0. To further resolve overlapping coordination shells, wavelet transform (WT) analysis of EXAFS oscillations was performed. The WT contour plot of Co displayed maxima at ≈4.5 and ≈7.72 $Å^{-1}$, corresponding to Co—N and Co—Co/Fe scattering paths, respectively (Figure 3j–m). Similarly, Fe WT plots showed distinct maxima at ≈3.9 and 7.6 $Å^{-1}$, indicative of Fe—N and Fe—Co/Fe coordination (Figure 3n–q). These findings highlight the structural and electronic synergy between Co and Fe centers, as well as nitrogen coordination [46]. This comprehensive spectroscopic analysis confirms that CNFC-3 comprises a hybrid architecture of CoFe alloy domains and metal–nitrogen coordination sites, which will collectively contribute to its enhanced electrocatalytic performance.

2.2 | Evaluation of Oxygen Electrocatalytic Activity

In pursuit of high-performance bifunctional oxygen electrocatalysts for energy conversion applications, ORR and OER activities of CoFe-based catalysts were evaluated. Using rotating disk electrode (RDE) measurements in O_2-saturated 0.1 M KOH, CNFC-3 exhibited a well-defined diffusion-limited current density (J_L) of 5.27 mA cm^{-2} at 1600 rpm, indicative of a dominant four-electron pathway (Figure 4a) [49, 50]. The catalyst delivered a half-wave potential ($E_{1/2}$) of 0.89 V vs RHE, outperforming NC (0.79 V), CN-NC (0.84 V), Fe-NC (0.845 V), CNFC-1 (0.868 V), CNFC-2 (0.864 V), and even commercial Pt/C (0.86 V) (Figure 4b),

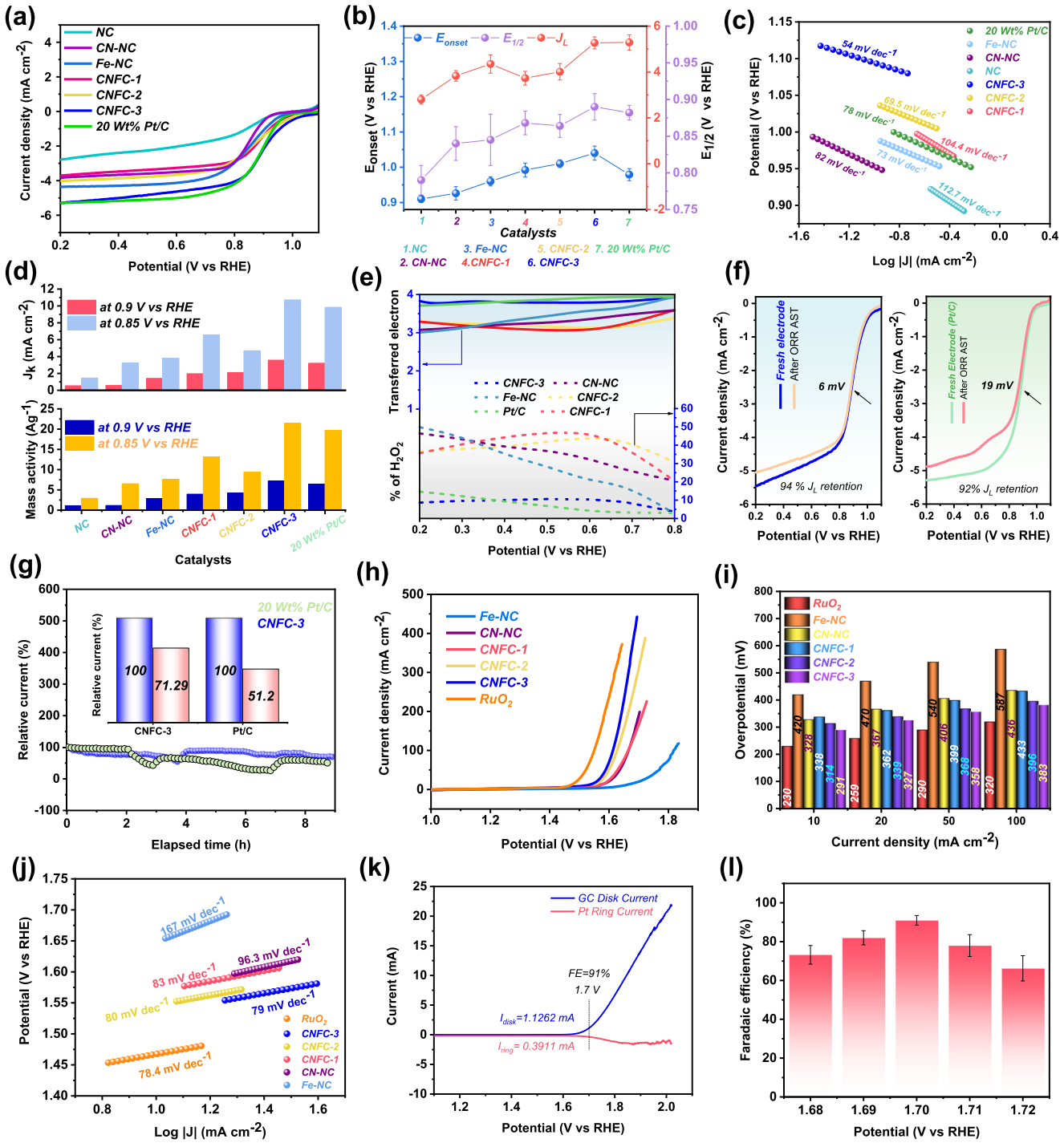

FIGURE 4 | (a) ORR LSV polarization curves of different catalyst in O_2 saturated 0.1 M KOH, (b) bar diagram shows that the variation of half-wave, onset, and limiting current density of different catalysts, (c) Tafel plot, (d) Kinetic current density and mass activity of different catalysts, (e) RRDE analysis showing the number of electron transfer and % of H_2O_2 formation of different catalysts at 1600 rpm in 0.1 M KOH, (f) ORR durability test, (g) chronoamperometric study showing the ORR activity retention over time (inset: comparison bar diagram of CNFC-3 and 20 wt% Pt/C), (h) OER LSV polarization curve of different catalysts in 1 M KOH, (i) bar diagram showing overpotential of different catalysts at different current densities, (j) Tafel plot, (k) Faradaic efficiency of CNFC-3 calculated from RRDE analysis at 1.7 V, (l) Faradaic efficiency of CNFC-3 at different potentials.

positioning CNFC-3 among the most active ORR catalysts of the decade (Table S5). Electrokinetic analysis revealed a Tafel slope of 54 mV dec^{-1}, comparable to that of Pt/C (78 mV dec^{-1}) and suggesting efficient reaction kinetics at the electrode–electrolyte interface (Figure 4c). To probe the intrinsic activity, the kinetic current density (J_k) of the catalysts was calculated, with CNFC-3 exhibiting significantly higher J_k across the entire kinetic control region (Figure 4d). At 0.85 V, CNFC-3 achieved a J_k value of 10.719 mA cm^{-2} outperforming NC (1.459 mA cm^{-2}), CN-NC (3.256 mA cm^{-2}), Fe-NC (3.806 mA cm^{-2}), CNFC-1 (6.576 mA cm^{-2}), CNFC-2 (4.682 mA cm^{-2}), and commercial Pt/C (9.837 mA cm^{-2}) (Figure 4d, upper). A similar trend was observed at 0.90 V.

This high J_k intuitively indicates the activation effect of multiple redox-active sites in CNFC-3. Additionally, CNFC-3 delivered a mass activity of 21.44 A g^{-1} at 0.85 V (Figure 4d, lower), representing a ≈1.1-fold improvement over Pt/C. Moreover, CNFC-3 synthesized at 800°C shows superior ORR activity compared to the catalyst synthesized at 700°C and follows a similar trend to CNFC-3 synthesized at 900°C (Figure S25). This result clearly indicates that the combination of alloy/nitride phase promotes the ORR activity. Rotating ring disk electrode (RRDE) measurements confirmed low H_2O_2 yield across a broad potential range, validating the four-electron pathway in case of CNFC-3 (Figure 4e and Figure S26a). Durability assessments under accelerated stress testing (AST) showed minimal $E_{1/2}$ decay (≈6 mV) and only a 6% decrease in J_L after 2000 CV cycles (Figure 4f, left). However, the Pt/C suffers from a greater $E_{1/2}$ decay and a lower J_L retention rate (≈92%) under identical experimental conditions, highlighting the low stability due to the high mobility of Pt on the carbon matrix (Figure 4f, right). Chronoamperometric measurements at 0.3 V in O_2-saturated 0.1 M KOH revealed that CNFC-3 retained 71.29% of its initial current density after 8 h, outperforming Pt/C (51.2%) (Figure 4g). Post-ORR ex situ TEM, HR-TEM, SAED, HAADF-STEM analysis (Figure S26b–p), attributes superior performance of CNFC-3 electrocatalyst to: 1) uniformly dispersed multiple active sites that modulate electronic structure and optimize oxygen intermediate adsorption; 2) enhanced triple-phase boundary efficiency via alloy/nitride decoration on carbon sheets/tubes; and 3) improved long-term stability and electron transport due to high graphitization and metal encapsulation.

OER performance is a critical criterion for rechargeable ZABs. The OER measurements were conducted in 1 M KOH electrolyte using a catalyst-loaded carbon cloth as the working electrode (catalyst loading was maintained at ≈1 mg cm^{-2}). CNFC-3 exhibited a sharp onset potential of ≈1.49 V vs RHE and delivered a current density of 10 mA cm^{-2} at 1.52 V (η_{10} = 290 mV), which is 60 mV higher compared to commercial RuO_2 (η_{10} = 230 mV) and outperforms other synthesized catalysts (Figure 4h). This OER performance is also comparable to that of state-of-the-art Co-based catalysts, and a detailed comparison of different highly active bifunctional catalysts is presented in Figure S27a,b and Table S5. CNFC-3 reached a high current density of 100 mA cm^{-2} at 383 mV overpotential, whereas RuO_2 required 320 mV (Figure 4i).

This superior activity is attributed to the synergistic effects of FeCo alloy nanoparticles and Co_4N on N-doped graphitic carbon. Double-layer capacitance (C_{dl}), derived from cyclic voltammetry in the non-Faradaic region (Figures S27c–g and S28) and electrochemically active surface area (EASA) measurements (Figure S29) further confirmed the intrinsic activity of CNFC-3 with C_{dl} of 19.74 mF cm^{-2} and EASA = 493.5 cm^2. Electrochemical impedance spectroscopy (EIS) revealed the lowest charge transfer resistance (R_{ct} = 13.7 Ω) for CNFC-3, indicating rapid proton-coupled electron transfer (Figure S30). The Tafel slope of CNFC-3 (79 mV dec^{-1}) was slightly higher than RuO_2 (78.4 mV dec^{-1}) yet lower than CNFC-2 (80 mV dec^{-1}), CN-NC (96.3 mV dec^{-1}), CNFC-1 (83 mV dec^{-1}), and Fe-NC (167 mV dec^{-1}) (Figure 4j), suggesting favorable OER kinetics. The Faradaic efficiency (FE) for OER was determined at 1.7 V vs. RHE using a RRDE [51]. The oxygen generated at the disk electrode was subsequently detected by reducing it at the ring electrode through a potential sweep (Figure 4k). Based on the ratio of the ring (I_{ring}) to disk (I_{disk}) currents, FE was calculated to be 91%. Furthermore, the variation of Faradaic efficiency with applied potential indicates that the maximum value is attained at ≈1.7 V vs RHE (Figure 4l). For the utilization of electrocatalysts in energy conversion/storage systems, the durability of the electrocatalyst is considered a key parameter that governs long-term practical application. The polarization curve obtained after 1000 CV cycles of the CNFC-3-based electrode material verifies the electrocatalytic stability towards OER (Figure S31a). Complementary ex situ TEM conducted post-OER further corroborates the structural integrity of the catalyst, revealing preserved morphology alongside partial surface reconstruction (Figure S31b–p). The enhanced OER performance of CNFC-3 is attributed to a synergistic interplay of structural and electronic factors: 1) the metallic nature of Co_4N and CoFe phases promotes efficient charge transfer between the current collector and the catalyst interface, facilitated by the conductive N-doped graphitic carbon tube framework; 2) the homogeneous dispersion of CoFe alloy and Co_4N nanoparticles across the porous carbon matrix increases the electrochemically active surface area, thereby improving electrolyte accessibility and intensifying interactions between catalytic sites and reaction intermediates; and 3) the formation of Co_4N/CoFe nanoscale heterojunctions induces electronic redistribution, modulating d-orbital occupancy and generating additional surface-active sites, collectively contributing to the superior activity and durability of CNFC-3 under OER conditions.

2.3 | Catalyst Screening and Mechanistic Elucidation

From TEM, HRTEM, HAADF-STEM, EELS line-scan, XPS, and XAS analyses, it is confirmed that alloy/nitride-based heterostructures are the experimentally dominant and catalytically relevant structures in this system. Here, the atomically dispersed sites are expected to modulate interfacial electronic structure and facilitate synergistic interactions, rather than act as the sole active centers. So, the present density functional theory (DFT) calculations were rationally focused on Co/Fe-based nanoclusters and Co_4N/CoFe heterointerfaces to obtain atomic-level mechanistic insights [52–58]. As an initial screening, five nanocluster-based catalysts models denoted as-Co@NC, Fe@NC, CoFe@NC, Co_4N@NC, and Co_4N/CoFe@NC were systematically investigated (Figure S32). These models consist of cobalt and iron clusters anchored onto nitrogen-doped graphitic carbon (NC), each pre-adsorbed with hydroxyl species [52]. Comprehensive electronic structure analysis, adsorption energy profiling, and charge transfer evaluations were employed to assess catalytic activity. The calculated d-band occupancies are 99.83 for Co@NC, 97.70 for Fe@NC, 93.93 for CoFe@NC, 150.67 for Co_4N@NC, 152.77 for CNFC-1, and 153.04 for CNFC-3 (Figure S33). Moreover, density of states (DOS) analysis revealed that in the case of CNFC-3, the d-band center (ε_d) is closer to the Fermi level, along with elevated d-band occupancy up to the Fermi level (O_d) (Figure S33). This electronic configuration of CNFC-3 facilitates stronger bonding with O_2 by minimizing antibonding orbital occupation, thereby enhancing charge transfer compared to the other catalysts [58]. Moreover, all catalyst structures were fully optimized to their lowest energy configurations, with atomic coordinates provided in Tables S6–S10. Binding energy

calculations confirmed thermodynamic stability, as all systems exhibited negative binding energies with the NC substrate, indicating robust anchoring to the N-doped carbon support (Figure S34) [53]. To identify the most promising catalyst among the studied systems, the limiting potentials for both the OER and ORR were computed across 20 active sites (Figures S35–S45). Bader charge analysis further revealed that sites with higher electronic charge density correlated strongly with superior catalytic performance (Figure S46). Adsorption energies of key OER/ORR intermediates (O*, OH*, and OOH*) were also evaluated, and the relationships between ΔG_{OOH}-ΔG_O and ΔG_{OH} displayed a volcano-type trend when plotted against the respective limiting potentials, highlighting the correlation between adsorption energy and catalytic activity (Figure S47). Catalytic activity under alkaline conditions was quantified by calculating Gibbs free energy changes (ΔG) for the four elementary steps of the OER and ORR, using the computational hydrogen electrode (CHE) model. The OER pathway proceeds via a series of proton-coupled electron transfer (PCET) steps, as illustrated in Figure S48 [54]:

$$* + 4OH^- \rightarrow OH^* \rightarrow O^* \rightarrow OOH^* \rightarrow * + O_2 + 2H_2O$$

Similarly, the ORR follows a four-electron transfer pathway, described by

$$* + O_2 + 2H_2O \rightarrow OOH^* \rightarrow O^* \rightarrow OH^* \rightarrow * + 4OH^-$$

Here, * represents adsorbed intermediates on the catalyst surface. For simplicity, free molecules are omitted from these equations; the complete forms are provided in the Supporting Information. Analysis revealed that, on the Co@NC system, the Co-2 site has the least OER overpotential of 1.38 V, while the Co3 site shows the lowest ORR overpotential of 1.92 V among all active sites in this material (Figure S49). In the Fe@NC system, the Fe-1 site exhibits superior bifunctional performance, with the lowest overpotentials for both OER and ORR, at 1.07 V and 1.38 V, respectively (Figure S49). For the bimetallic CoFe@NC catalyst, the Co-1 site shows the most favorable OER overpotential of 1.68 V, while the Fe-2 site records an ORR overpotential of 1.82 V (Figure S49). Similarly, in the Co_4N@NC structure, the Co_3 site achieves the lowest OER overpotential of 1.31 V, and the Co-1 site displays the best ORR performance with an overpotential of 1.54 V (Figure S49). Despite these promising features, the overall electrocatalytic activities of the individual systems remain suboptimal (Figure S35). To overcome this, a hybrid CNFC structure was designed by integrating Co_4N and CoFe alloy clusters to synergistically enhance catalytic performance (Figure 5a) [55]. The charge density difference plot for the CNFC system reveals distinct regions of charge accumulation and depletion around the nanocluster, indicating effective charge transfer between the active sites and the NC support (Figure 5b). In addition, ab initio molecular dynamics (AIMD) simulations performed at 350 K for up to 10 000 fs demonstrate minimal structural fluctuations at high temperatures, confirming the thermodynamic stability of the hybrid electrocatalyst (Figure 5c) [56]. Adsorption energy calculations further support its superior catalytic performance: the Co-2 (Co214) site exhibits the lowest OER overpotential of 0.65 V, while the Fe-2 site achieves the lowest ORR overpotential of just 0.47 V, outperforming the other studied systems (Figure 5d,e, and Figures S36–S45). These findings collectively demonstrate that CNFC-3 possesses exceptional bifunctional catalytic activity and stability, making it a highly promising candidate for ZAB applications. Bader charge analysis, charge density difference plots, crystal orbital Hamilton population (COHP), and projected density of states (PDOS) were evaluated to understand the role of the Co-2 and Fe-2 sites in the CNFC-3 system for enhanced oxygen electrocatalytic activity. Charge density difference plots and Bader charge analysis reveal substantial charge transfer from the Co-2 and Fe-2 sites to adsorbed intermediates (*O, *OH, *OOH), with transferred charges of 0.319 e, 0.239 e, and 0.299 e at Co-2, and 0.203 e, 0.359 e, and 0.301 e at Fe-2, respectively (Figure 5f and Tables S11 and S12), where yellow color represents areas of charge accumulation and cyan blue color shows charge depletion [57]. These findings indicate strong adsorption and optimal interaction with oxygenated species. The PDOS analysis, COHP, and integrated COHP analysis of the Co-2 and Fe-2 sites further provide deeper insights into the underlying atomic-level electronic interactions and intermediate binding phenomena (Figure 5g–j). The PDOS analysis reveals a reduction in d-orbital electronic occupancy upon intermediate adsorption, indicating charge transfer from the metal sites to the adsorbed molecules (Figure 5i,j). The d-band occupancy, defined as $O_d = \int_{-\infty}^{E_F} D_d(E)\, dE$, decreased on the Co-2 site from 7.4601(pristine) to 7.3611, 7.3916, and 7.3896 after the adsorption of *O, *OH, and *OOH, respectively (Figure 5i). Similarly, for the Fe-2 site, the occupancy reduced from 6.2467 to 6.2100, 6.1670, and 6.2072 upon adsorption of the same intermediates (Figure 5j) [3]. This decline in d-electron occupancy signifies effective orbital interaction and electron donation from the active sites to the adsorbates, further confirming its strong catalytic interaction [57]. The d-band centers of both sites lie closer to the Fermi level prior to intermediate adsorption, facilitating strong bonding with minimal antibonding state occupancy [58].

COHP and integrated COHP (ICOHP) analyses corroborate these findings. The COHP plots for the Co-2 and Fe-2 sites, following the adsorption of *O, *OH, and *OOH, clearly show very low occupancy of antibonding states. Furthermore, the ICOHP values are negative (Figure 5g,h), confirming the presence of optimum bonding interactions between the adsorbed oxygen species and the active metal sites in CNFC-3. Again, more negative ICOHP values indicate stronger bonding due to the lower occupancy of the antibonding electrons. In the case of OER on the Co-2 site, the OOH bond is the strongest, as evidenced by the ICOHP value of -1.39427, the most negative among the Co—O bonds. This step is therefore the rate-determining step of the OER reaction, as evidenced by the free energy profile (Figure 5d). Similarly, for ORR on the Fe-2 site, the bonding between *O and the Fe-2 site is the rate-determining step. Notably, the ICOHP value of -1.75984 is the most negative among evaluated sites, indicating the strongest bond and further confirming its role as the rate-determining step in the ORR process (Figure 5e,h) [59]. To examine the role of interfacial proximity, we introduced spatial separation between Co_4N and CoFe in a without heterointerfacial CNFC-1 model (Figure S50). This configuration led to increased OER and ORR limiting potentials (0.94 V and 0.87 V, respectively) for Co-2 and Fe-2 sites (Figure 5k,l). The reduced ICOHP values (-1.27619 to -1.02577) at the Co-2 site upon OH adsorption indicates weaker bonding and higher antibonding occupancy in CNFC-1 compared to the lower antibonding character observed in CNFC-3 (Figure S51). Furthermore, the PDOS and COHP analyses of the

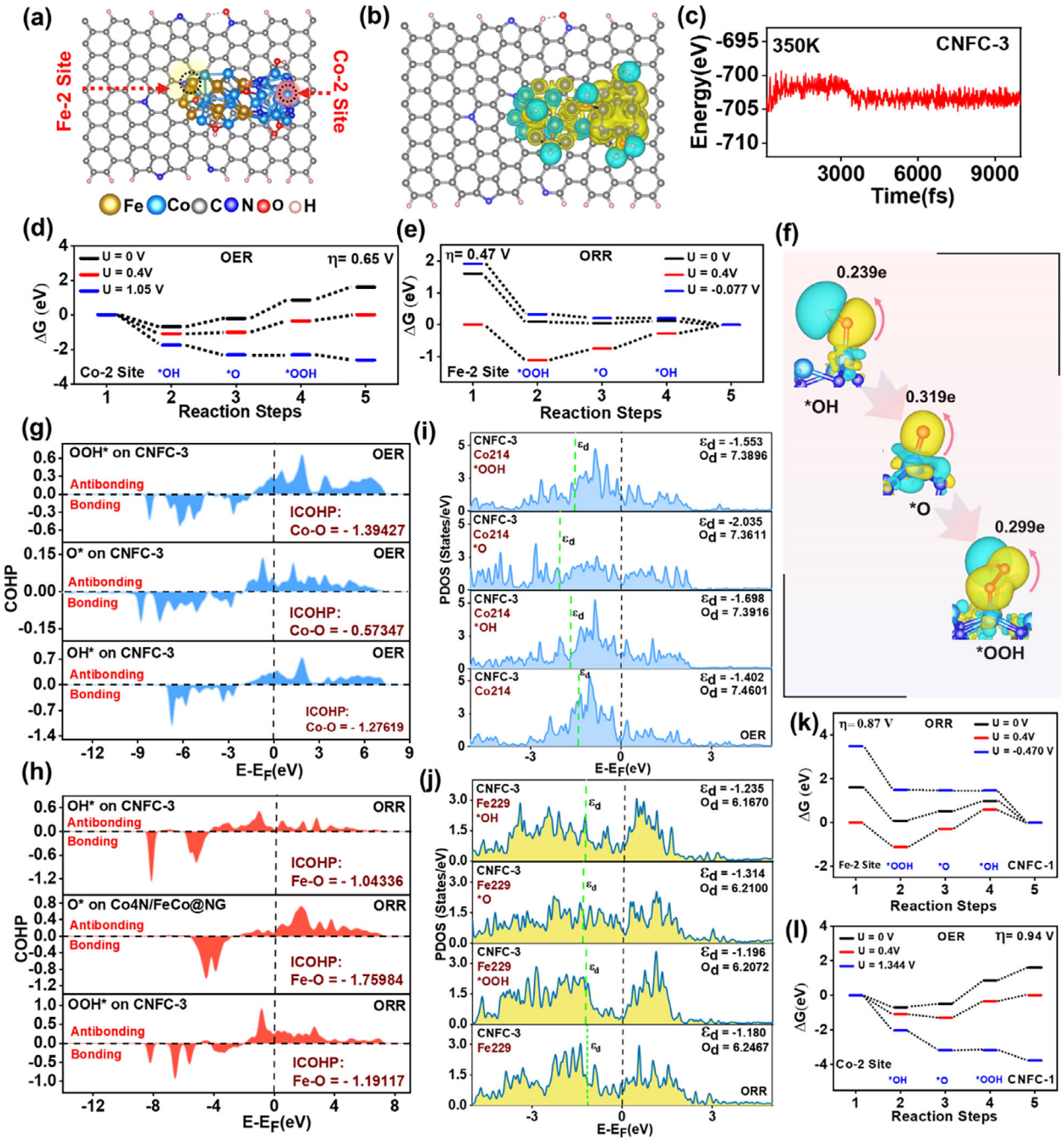

FIGURE 5 | (a) Optimized atomic structure of the CNFC-3 catalyst, highlighting the active sites Co-2 and Fe-2 which are Co214 and Fe229 respectively, (b) charge density difference mapping of CNFC-3, (c) ab initio molecular dynamics (AIMD) simulation of CNFC-3 at 350 K, confirming structural stability, (d) free energy profile for the oxygen evolution reaction (OER) at the Co-2 active site, (e) free energy profile for the oxygen reduction reaction (ORR) at the Fe-2 site, (f) charge density difference plots at the Co-2 site following the adsorption of O, OH, and OOH intermediates, (g) crystal orbital Hamilton population (COHP) analysis of the Co-2 site after O, OH, and OOH adsorption, (h) COHP plot for the Fe-2 site after adsorption of O, OH, and OOH, (i) partial density of states (PDOS) of the Co-2 site before and after adsorption of OER intermediates (O, OH, OOH), (j) PDOS analysis at the Fe-2 site before and after adsorption of ORR intermediates, (k) free energy profile of the ORR at the Fe-2 site within the long range CNFC-1 system, (l) free energy profile of the OER at the Co-2 site within the extended CNFC-1 (without heterointerfacial) system.

heterointerface (Figures S52 and S53) reveal a robust Fe—Co interaction (ICOHP of -0.8845) alongside distinct Fe—N orbital hybridization at the interface. These results confirm that the heterointerfacial interface in CNFC-3 modulates d-orbital occupancy and optimizes M—O bonding, positioning the catalyst near the apex of the OER/ORR volcano plot. Collectively, these findings establish CNFC-3 as a thermodynamically stable, electronically tuned, and structurally robust bifunctional electrocatalyst, offering a promising platform for next-generation ZAB applications.

2.4 | Electrochemical Performance Analysis of Aqueous ZAB

A key criterion for evaluating air-electrode efficacy in ZABs is the oxygen redox potential gap ($\Delta E = E_{j\ =\ 10}\text{-}E_{1/2}$), which directly influences rechargeability. The CNFC-3 catalyst exhibits a ΔE of ≈ 0.631 V, closely matching the benchmark Pt/C-RuO_2 couple (Figure S54) and aligning with leading air–electrode materials (Figure S27a,b and Table S5). Encouraged by its favorable oxygen reversibility under alkaline conditions, CNFC-3 was employed as the air electrode in both aqueous and semi-solid flexible ZAB configurations. The mechanism of ZABs in alkaline conditions is schematically portrayed in Figure 6a. To benchmark performance, a reference ZAB incorporating Pt/C was used to assess power density and specific capacity, while a Pt/C-RuO_2-based system served for rechargeability comparisons. For aqueous ZAB, CNFC-3 was loaded (loading: ≈ 3 mg cm^{-2}) onto carbon paper as an air-cathode, paired with a Zn foil anode and an electrolyte comprising 6.0 M KOH + 0.2 M Zn $(Ac)_2$. The CNFC-3-based primary ZAB achieved an open circuit voltage (OCV) of 1.521 V (Figure 6b) which remained stable over a 10 min interval and exceeded that of the Pt/C-based counterpart (Figure 6c). Under galvanostatic discharge, the CNFC-3-based ZAB demonstrated a peak power density of ≈201 mW cm^{-2} at 320.3 mA cm^{-2} and excellent specific capacity of 812 mAh g_{Zn}^{-1} at current density of 50 mA cm^{-2} (Figure 6d–f), approaching the theoretical limit of 820 mAh g_{Zn}^{-1}. Compared to the Pt/C reference ZAB (power density ≈151.84 mW cm^{-2} at 286.9 mA cm^{-2}, capacity ≈742.6 mAh g_{Zn}^{-1}), CNFC-3 outperformed in both energy output and efficiency, comparable with the recently reported ZABs (Table S13). Notably, the CNFC-3-based system achieved an energy density of 877 Wh kg^{-1}, which is 1.13 times greater than the Pt/C based reference ZAB (Figure S55a). These metrics are advantageous for ampere-hour-scale applications, which are discussed in Figure S55. Voltage profiles during charge–discharge cycling revealed a narrower voltage gap for CNFC-3 relative to Pt/C-RuO_2 (Figure 6e), indicative of superior reversible oxygen electrocatalytic activity. This trend was consistent across varying current densities. Rate capability was further validated via constant current-constant time (CC-CT) analysis (Figure 6g), where CNFC-3 consistently maintained higher discharge plateaus across all current densities, with the performance gap widening at elevated currents. This discharge behavior validates the efficacy of CNFC-3 in ORR kinetics. Long-term cycling stability was assessed via galvanostatic charge-discharge tests at 5 mA cm^{-2} (10 min per cycle, Figure 6h), revealing stable operation over 115 h with minimal voltage degradation (Figure 6j,k). In contrast, the Pt/C-RuO_2 system exhibited a rapid voltage gap increase from 0.82 to 1.409 V within 50 h (Figure 6h). At a high current density of 20 mA cm^{-2}, the CNFC-3-based ZAB maintained a depth of discharge per cycle (DoDc) of 2.851%, and after 100 cycles, showed only a 3.97% decline in round-trip voltaic efficiency (RTVE) (Figure 6l), affirming its robustness and reversibility under demanding conditions. Moreover, the decay rate in the RTVE (0.022% per cycle at 5 mA cm^{-2} and 0.127% at 20 mA cm^{-2}) is shown in Figure 6m,n. Cycling performance at high current density (50 mA cm^{-2}) and elevated areal capacity (25 mAh cm^{-2}) serves as a critical benchmark for assessing the practical viability of ZABs.

Remarkably, the CNFC-3-based air-electrode exhibits outstanding stability under these demanding conditions, sustaining a DoDc of 47.773% while maintaining a stable voltage gap of 1.14 V and a RTVE of 48.18% across 12 cycles (Figure 6o). When benchmarked against state-of-the-art ZAB systems, the electrochemical metrics of CNFC-3 affirm its position as a high-performance electrode material, well-suited for next-generation ZAB applications (Table S13).

2.5 | Electrochemical Performance Analysis of Quasi-Solid-State-Flexible ZAB (QSSFZB)

The pronounced reversibility of the CNFC-3 electrode in liquid-phase Zn–air cells prompted its integration into a QSSFZB architecture. A key challenge in realizing such flexible energy storage systems lies in engineering aqueous polymer electrolytes that simultaneously exhibit mechanical robustness and thermal adaptability. The electrochemical behavior of water-based gel polymer electrolytes across temperature regimes is largely dictated by the interplay among water molecules, ionic species, and the polymer matrix, particularly its structural backbone and terminal functionalities [60–62]. To address these constraints, a novel gel electrolyte incorporating nitrilotriacetic acid (NTA) into a poly(acrylic acid)-poly(acrylamide) (PAA-NTA-PAM, denoted as P-P-N) framework was synthesized (Figure S56) and subsequently infused with 6 M KOH+0.2 M Zn $(Ac)_2$ prior to QSSFZB assembly. The resulting P-P-N gel electrolyte showed excellent mechanical flexibility and strong adhesion to diverse substrates, confirming its suitability for flexible device integration (Video S2). To elucidate the role of NTA, a control gel electrolyte composed of PAA-PAM (P-P) was also prepared. Initial ionic conductivity measurements revealed a value of 50.22 mS cm^{-1} (Figure S57) for the P-P gel, which increased to 69.66 mS cm^{-1} upon NTA incorporation, highlighting its facilitative effect. This enhancement is attributed to the three terminal carboxylate groups in NTA, which likely reinforce the hydrogen-bonding network within the electrolyte matrix, thereby promoting ion mobility. EIS of P-P-N gel immersed in KOH and Zn $(Ac)_2$ solution revealed temperature-dependent ionic conductivities of 15.4 mS cm^{-1} at ≈0°C, 141.8 mS cm^{-1} at 27°C, and 156.3 mS cm^{-1} at 60°C (Figure S58). These results highlight the strong electrolyte retention of the gel and ion transport capabilities across a broad thermal range, affirming its potential for all-weather, quasi-solid-state Zn–air battery applications. Compatibility of electrolyte with the Zn anode was further assessed using a Zn||Zn symmetric cell configuration. As shown in Figure S59, the P-P-N gel showed reduced overpotential compared to its NTA-free counterpart, suggesting that NTA incorporation enhances Zn^{2+} coordination, facilitates ionic transport, and lowers interfacial resistance. These effects collectively contribute to improved Zn plating/stripping reversibility, likely mediated by the formation of a stable zincophilic interface.

Atomic force microscopy (AFM; Figure S60) and PXRD (Figure S61) analyses provide compelling evidence for NTA's stabilizing influence on Zn anode surface chemistry. Zn deposition facilitated by P-P-N gel electrolyte yields well-defined hexagonal close-packed (hcp) Zn reflections, predominantly along the (002) and (101) planes, indicative of uniform and oriented growth. In

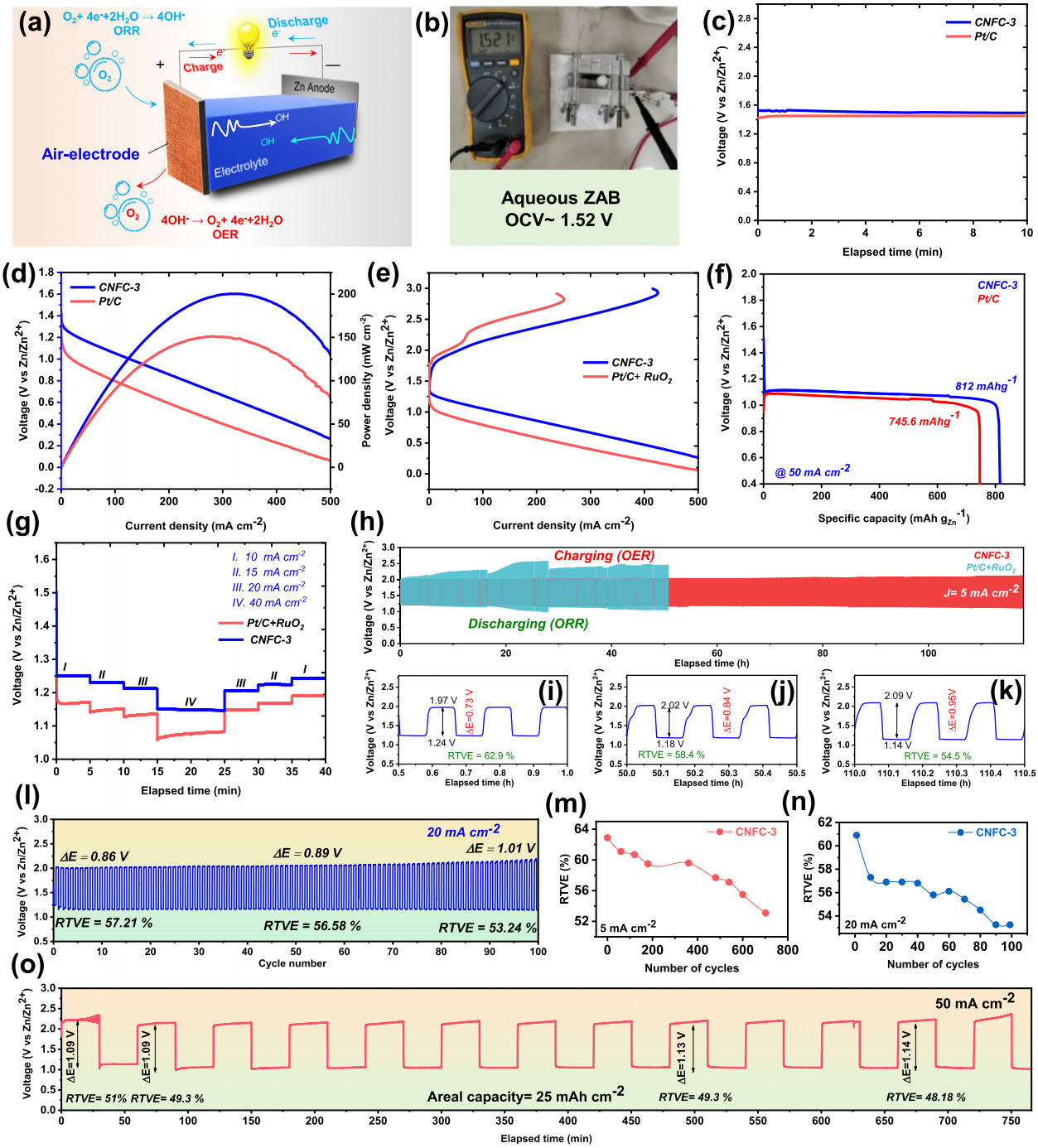

FIGURE 6 | (a) Schematic illustration of Zn-air battery, (b) digital image showing the OCV of CNFC-3 based ZAB, (c) long term OCV, (d) discharge-polarization, (e) charging-discharging polarization, (f) specific capacity, (g) rate performance analysis of CNFC-3 and Pt/C+RuO_2 based ZAB, (h) long term cycling stability, (i–k) variation of RTVE with cycling time, long-term Galvanostatic charge/discharge at (l) 20 mA cm^{-2} current density, (m,n) variation of RTVE at different current densities, (o) cycling stability at 50 mA cm^{-2}.

contrast, Zn anodes cycled with the NTA-free P-P gel exhibit broadened Zn peaks, accompanied by distinct ZnO and $Zn(OH)_2$ signatures, reflecting pronounced surface corrosion and dendritic growth. These observations affirm that NTA incorporation effectively suppresses parasitic side reactions and promotes dendrite-free, stable Zn deposition. The crystallographic preference for Zn growth along the (002) plane is quantitatively assessed using the intensity ratio I(002)/I(101), a commonly used metric for evaluating deposition orientation [61, 62]. The P-P-N-based system achieves an I (002)/I (101) ratio of 0.644, surpassing the 0.55 observed for P-P counterparts, further substantiating the role of NTA in directing uniform Zn nucleation and enhancing anode stability during extended cycling.

To elucidate the molecular-level interactions underpinning this behavior, spin-polarized density functional theory (DFT) calculations were performed to evaluate the interfacial energetics between the PAA-NTA-PAM electrolyte and Zn anode surfaces

(Figure S62). Among the crystallographic facets considered, Zn(001) exhibited superior thermodynamic stability with an optimized energy of -394.195 eV, compared to -355.114 eV for Zn(101) (Figure S63), and was thus selected for further analysis. AIMD simulations conducted at 200 K, 300 K, and 500 K, demonstrated the structural resilience of the PAA-NTA-PAM electrolyte under thermal stress (Figure 7a–c). To isolate the contribution of NTA to interfacial binding, comparative simulations were performed with and without the NTA moiety [63]. The Zn—O bond length was significantly reduced in the presence of NTA (2.21 Å) relative to the NTA-free system (2.55 Å), as illustrated in Figure 7d,e. This shortening reflects enhanced interfacial coordination, suggesting that NTA plays a pivotal role in strengthening electrolyte-anode interactions and mitigating dendrite formation through the establishment of a stable zincophilic interface [64].

Further analysis of the Zn(101) surface reveals that NTA plays a similarly critical role in modulating interfacial interactions. The Zn—O bond length is significantly shortened to 2.01Å with NTA incorporation, compared to 2.48 Å without it (Figure S63a,b), indicating stronger coordination. Charge density difference plots (Figure 7f,g) for the Zn(001)/electrolyte interface show distinct regions of charge accumulation and depletion, confirming robust electronic coupling. On the Zn(101) surface, similar charge accumulation is observed in the PAA-NTA-PAM@Zn(101) surface (Figure S63c,d), further supporting the enhanced interfacial interaction. COHP analysis provides quantitative insight into bond strength. The integrated COHP (ICOHP) value for the Zn(001)/PAA-NTA-PAM system is -1.02577, more negative than the -0.87694 observed for the Zn(001)/PAA-PAM system without NTA (Figure 7h,i).

Likewise, the Zn(101)/P-P-N interface exhibits an ICOHP of -1.24511, surpassing the -0.94513 of the NTA-free counterpart (Figure 7j and Figure S63e,f). These more negative ICOHP values confirm that NTA significantly strengthens Zn—O bonding, thereby enhancing electrolyte-anode adhesion and suppressing dendrite formation, key factors for long-term Zn–air battery stability [64, 65]. PDOS analysis further corroborates these findings, revealing clear orbital hybridization between Zn atoms and coordinating oxygen atoms in the electrolyte (Figure S64). Collectively, these electronic structure insights, including charge density mapping, bond length analysis, and COHP/PDOS evaluations, emphasize the pivotal role of the PAA-NTA-PAM framework in facilitating efficient charge transfer and stable electrode-electrolyte interactions.

The CNFC-3-based QSSFZB demonstrates superior electrochemical performance, delivering a stable open-circuit voltage (OCV) of ≈1.47 V, exceeding the ≈1.42 V of the Pt/C-based reference device (Figure 7k; Figure S65). At ambient temperature, the CNFC-3-based QSSFZB achieves a peak power density of 94 mW cm^{-2} (Figure 7l), outperforming the Pt/C-based system (81 mW cm^{-2}). EIS profiles (Figure S66) reveal reduced charge-transfer resistance, consistent with enhanced reaction kinetics and improved discharge polarization behavior.

To assess thermal adaptability, QSSFZB performance was evaluated across a temperature range (≈0, 27, and 65°C). The device maintains power densities of 33.2 mW cm^{-2} at ≈0°C, 94 mW cm^{-2} at 27°C, and 53.2 mW cm^{-2} at 60°C (Figure 7m), surpassing the low-temperature performance of several reported systems (Table S14). The observed decline in power output at temperature extremes is attributed to distinct limiting mechanisms: at low temperatures, reduced ionic mobility and sluggish ORR kinetics hinder performance; at elevated temperatures, although ionic transport is enhanced, increased peroxide intermediate formation favors the less efficient two-electron ORR pathway, compromising energy conversion efficiency [66, 67]. Despite these thermal challenges, the CNFC-3-based QSSFZB exhibits excellent cycling stability. Over 300 cycles at 5 mA cm^{-2}, the RTVE remains between 52.3% and 39.6% (Figure 7n), reflecting the durability of the bifunctional catalyst. Post-cycling power density decreases to 24.1 mW cm^{-2} (Figure S67a), and EIS spectra indicate increased charge-transfer resistance due to prolonged electrochemical stress (Figure S67b). Ex situ XRD analysis confirms structural integrity of the air-cathode, with minimal changes in PXRD patterns (Figure S68). However, the emergence of new peaks corresponding to CoOOH, FeOOH, and K_2CO_3 (PDF No: 01-1001) suggests surface reconstruction and by-product formation during extended cycling. To further validate high-rate performance, QSSFZBs were tested at 10 mA cm^{-2} and 0.57% *DoDc*, outperforming several reported systems (Table S14). The device sustains over 145 cycles (2 min charge/2 min discharge) with RTVE declining modestly from 49.4% at cycle 2 to 35.5% at 148 cycles (Figure 7o), demonstrating excellent rechargeability and long-term operational stability. Mechanical flexibility was assessed through bending tests at various angles (0°, 45°, 90°, 180°, and reverse), with negligible impact on energy efficiency (Figure 7p, Figure S69), confirming the suitability of the device for wearable applications. The discharge curve (Figure 7q) reveals a high voltage plateau and a specific capacity of 551.2 mAh g_{Zn}^{-1} at 10 mA $cm^{-2,}$ indicating efficient Zn utilization. Across a range of current densities (2, 4, 10, and 15 mA cm^{-2}), the CNFC-3-based QSSFZB consistently delivers higher discharge voltages than the Pt/C-based counterpart (Figure 7r). Notably, upon reverting to 2 mA cm^{-2}, the discharge voltage recovers to 96.7% of its initial value, attesting to the device's electrochemical reversibility and resilience under dynamic operating conditions.

However, the QSSFZB performance is inferior to that of the aqueous rechargeable ZAB. To address this concern comprehensively, combined experimental reasoning with molecular-level theoretical analysis was employed (Figures S70–S72). In summary, the CNFC-3-based QSSFZB developed through a comprehensive optimization strategy, exhibits exceptional electrochemical performance, mechanical robustness, and environmental adaptability. Its stable operation under extreme conditions and compatibility with flexible form factors position it as a promising candidate for next-generation wearable electronics and compact portable energy systems (Figure S73 and Videos S3 and S4).

3 | Conclusions

In this work, we have demonstrated a dual N-source-assisted partial nitridation strategy to rationally tune the Co_4N/CoFe interfaces encapsulated within a graphitic N-doped carbon matrix (CNFC-3). CNFC-3 exhibited a high ORR half-wave potential of 0.89 V, a small ΔE gap of ≈0.631 V, and a low Tafel slope (54 mV dec^{-1} for ORR and 79 mV dec^{-1} for OER), outperforming

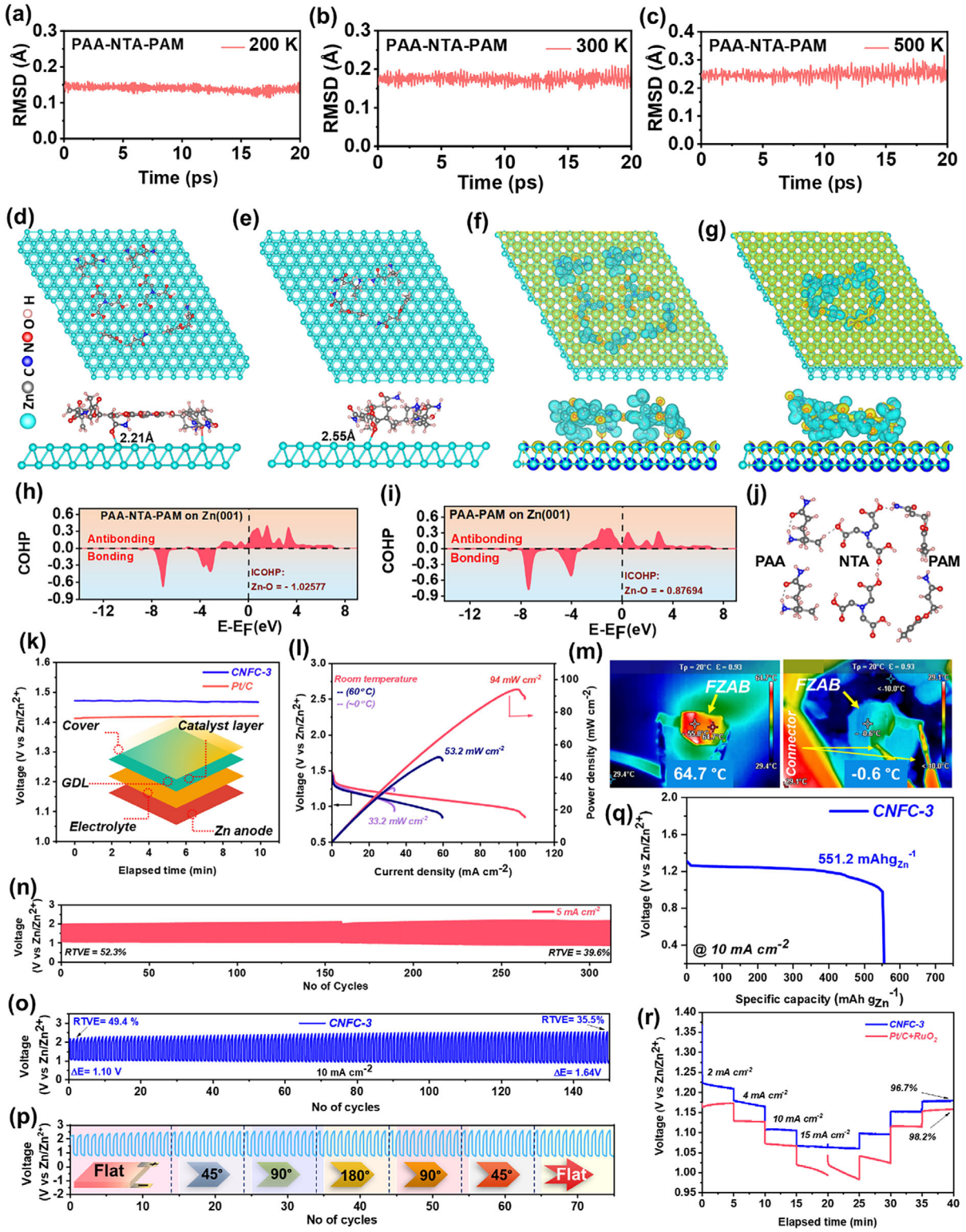

FIGURE 7 | (a–c) Ab initio molecular dynamics (AIMD) simulation snapshots of PAA-NTA-PAM at 200, 300, and 500 K, respectively, demonstrating thermal stability, (d) optimized atomic structure of the PAA-NTA-PAM polymer electrolyte on the Zn(001) surface, (e) optimized structure of PAA-PAM (without NTA) on Zn(001), (f, g) charge density difference plots of PAA-NTA-PAM@Zn(001) and PAA-PAM@Zn(001), respectively, showing regions of charge accumulation and depletion at the interface, (h, i) Crystal orbital Hamilton population (COHP) plots of PAA-NTA-PAM@Zn(001) and PAA-PAM@Zn(001), respectively, revealing the bonding interactions between Zn and O, (j) optimized structure of the stand-alone PAA-NTA-PAM electrolyte, (k) OCV plot of CNFC-3 and Pt/C based QSSFZBs, (l) Discharge polarization and corresponding power density plot of CNFC-3 based ZAB at Low, room and high temperature (m) real-time infrared thermal sensitivity images of the CNFC-3 based QSSFZB, (n) long term charge-discharge cycling stability of the CNFC-3 based QSSFZB at 5 mA cm^{-2}, (o) 10 mA cm^{-2}, (p) charging-discharging test under various mechanical stress at 10 mA cm^{-2}, (q) discharge capacity of CNFC-3 based QSSFZB, (r) rate performance at different current densities (2–15 mA cm^{-2}).

state-of-the-art catalysts (Table S5). The excellent bifunctional activity is primarily attributed to the optimized architecture, which facilitates orbital coupling and precise modulation of d-orbital occupancy, both of which are beneficial for optimal binding to oxygenated intermediates. As expected, the CNFC-3-based aqueous ZAB exhibited a lower charge discharge potential gap at 100 mA cm^{-2}, superior power density (201 mW cm^{-2}), specific capacity, and excellent cycling durability compared to the Pt/C+RuO_2 based ZAB at variable current densities (5, 10 mA, and 50 mA cm^{-2}) with negligible change in RTVE. Furthermore, as fabricated in-house, Ah-scale ZAB exhibited a power output of up to ≈ 2.38 W and stable rate performance at the ampere scale. Besides, the P-P-N gel-electrolyte with CNFC-3 based QSSFZB delivered an OCV of 1.47 V, peak power density of 94 mW cm^{-2}, and specific capacity of 551.2 mAh g_{Zn}^{-1}. The remarkable temperature tolerance, rate capability, cycling stability at high current density, and mechanical flexibility validate the formation of a stable anode–electrolyte interface. This study not only orchestrates d-orbital tuning in nitride-alloy systems but also opens new horizons for next-generation high-performance air electrodes in all-solid-state Zn–air batteries.

Acknowledgements

This work received financial support from the Department of Science and Technology, New Delhi, Govt. of India (DST/INSPIRE/04/2020/000616). S.D. is grateful to the CSIR, Govt. of India, for the CSIR SRF-Direct Fellowship File No: 31/0019(23452)/2025-EMR-I. T.K. is thankful to the CMPDI Project, Sanction No. CU-61/04 dated 08.01.2024 for financial assistance. A.K. acknowledges financial support from the DST-INSPIRE Faculty Scheme. A.P., S.M., and R.T. gratefully acknowledge the National Supercomputing Mission (NSM), India, for providing access to the PARAM Porul supercomputing facility, and SRM University-AP, Andhra Pradesh, for access to centralized computational resources. R.T. also thankful to the Science and Engineering Research Board (SERB), India (Grant no. CRG/2022/005423). The authors are thankful to Dr. Biplab Ghosh, Beamline Development & Application Section, Bhabha Atomic Research Centre (BARC), Trombay, Mumbai for the XAS measurements and SATHI Foundation IIT Kharagpur for providing STEM and EELS facility. Dr. A.K. also acknowledges the SEED research grant (SRMAP/URG/SEED/2025-26/053) provided by SRM University-AP, Andhra Pradesh and the central research facility.

Conflicts of Interest

The authors declare no conflicts of interest.

Data Availability Statement

The data that support the findings of this study are available on request from the corresponding author. The data are not publicly available due to privacy or ethical restrictions.

References

1. S. S. Shinde, S.-H. Kim, N. K. Wagh, and J.-H. Lee, "Design Strategies for Practical Zinc-Air Batteries toward Electric Vehicles and beyond," *Advanced Energy Materials* 15 (2025): 2405326, https://doi.org/10.1002/aenm.202405326.

2. T. Gu, Y. Jia, L. Zhang, et al., "Ampere-Hour-Scale Quasi-Solid-State Zinc–Air Batteries with a Wide Operating Temperature Range (−50 to 60°C)," *Journal of the American Chemical Society* 147 (2025): 15029–15040, https://doi.org/10.1021/jacs.4c16807.

3. S. Das, A. Pathak, U. Phadikar, et al., "Harnessing the Trade-off between CoFe/Fe_3C Interfacial Junction with Unparalleled Potential Gap of 0.58 V for Reversible Oxygen Electrocatalysis: Application toward Liquid and Solid-State Zn-Air Batteries," *Advanced Functional Materials* 34 (2024): 2407078, https://doi.org/10.1002/adfm.202407078.

4. S. Das, S. Bolar, E. E. Siddharthan, et al., "Pyridinic-N Seized Co in Biphasic Nanoarchitecture for Reversible Oxygen Electrocatalysis Enabling Longevous (>1200 h) Aqueous and Dual-Anion Kosmotropic Electrolyte Stabilized High Power Quasisolid-State Zn–Air Battery," *Small Methods* 9 (2025): 2401874, https://doi.org/10.1002/smtd.202401874.

5. A. Kundu, T. Kuila, N. C. Murmu, P. Samanta, and S. Das, "Metal–organic Framework-Derived Advanced Oxygen Electrocatalysts as Air-Cathodes for Zn–Air Batteries: Recent Trends and Future Perspectives," *Materials Horizons* 10 (2023): 745–787, https://doi.org/10.1039/D2MH01067D.

6. Y. Zheng, D. Wu, T. Wang, Q. Liu, and D. Jia, "Advanced Eutectogel Electrolyte for High-Performance and Wide-Temperature Flexible Zinc-Air Batteries," *Angewandte Chemie International Edition* 64 (2025): 202418223, https://doi.org/10.1002/anie.202418223.

7. Y. Wang, T. Yang, X. Fan, et al., "Anchoring Fe Species on the Highly Curved Surface of S and N Co-Doped Carbonaceous Nanosprings for Oxygen Electrocatalysis and a Flexible Zinc-Air Battery," *Angewandte Chemie International Edition* 63 (2024): 202313034, https://doi.org/10.1002/anie.202313034.

8. H. Wang, J. Li, K. Li, et al., "Transition Metal Nitrides for Electrochemical Energy Applications," *Chemical Society Reviews* 50 (2021): 1354–1390, https://doi.org/10.1039/D0CS00415D.

9. Y. Xiong, Y. Yang, F. J. DiSalvo, and H. D. Abruña, "Metal–Organic-Framework-Derived Co–Fe Bimetallic Oxygen Reduction Electrocatalysts for Alkaline Fuel Cells," *Journal of the American Chemical Society* 141 (2019): 10744–10750, https://doi.org/10.1021/jacs.9b03561.

10. Q. Shi, Q. Liu, Y. Ma, et al., "High-Performance Trifunctional Electrocatalysts Based on FeCo/Co_2P Hybrid Nanoparticles for Zinc–Air Battery and Self-Powered Overall Water Splitting," *Advanced Energy Materials* 10 (2020): 1903854, https://doi.org/10.1002/aenm.201903854.

11. H. Liu, D.-H. Yang, X.-Y. Wang, J. Zhang, and B.-H. Han, "N-Doped Graphitic Carbon Shell-Encapsulated FeCo Alloy Derived from Metal–polyphenol Network and Melamine Sponge for Oxygen Reduction, Oxygen Evolution, and Hydrogen Evolution Reactions in Alkaline media," *Journal of Colloid and Interface Science* 581 (2021): 362–373, https://doi.org/10.1016/j.jcis.2020.07.055.

12. B. Wang, K. Srinivas, Y. Liu, et al., "N-Doped CNTs Capped with Carbon Layer Armored CoFe Alloy as Highly Stable Bifunctional Catalyst for Oxygen Electrocatalysis," *Nano Research* 15 (2022): 3971–3979, https://doi.org/10.1007/s12274-022-4084-1.

13. K. Kim, K. Min, Y. Go, et al., "FeCo Alloy Nanoparticles Embedded in N-Doped Carbon Supported on Highly Defective ketjenblack as Effective Bifunctional Electrocatalysts for Rechargeable Zn–Air Batteries," *Applied Catalysis B: Environmental* 315 (2022): 121501, https://doi.org/10.1016/j.apcatb.2022.121501.

14. W. Yuan, S. Wang, Y. Ma, Y. Qiu, Y. An, and L. Cheng, "Interfacial Engineering of Cobalt Nitrides and Mesoporous Nitrogen-Doped Carbon: Toward Efficient Overall Water-Splitting Activity with Enhanced Charge-Transfer Efficiency," *ACS Energy Letters* 5 (2020): 692–700, https://doi.org/10.1021/acsenergylett.0c00116.

15. K. Oda, T. Yoshio, and K. Oda, "Preparation of Co-N Films by RF-Sputtering," *Journal of Materials Science* 22 (1987): 2729–2733, https://doi.org/10.1007/BF01086464.

16. P. Chen, K. Xu, Z. Fang, et al., "Metallic Co_4N Porous Nanowire Arrays Activated by Surface Oxidation as Electrocatalysts for the Oxygen Evolution Reaction," *Angewandte Chemie International Edition* 54 (2015): 14710–14714, https://doi.org/10.1002/anie.201506480.

17. G. Zhang, B. Y. Xia, and X. Wang, "Strongly Coupled $NiCo_2O_4$ -rGO Hybrid Nanosheets as a Methanol-Tolerant Electrocatalyst for the Oxygen

Reduction Reaction," *Advanced Materials* 26 (2014): 2408–2412, https://doi.org/10.1002/adma.201304683.

18. X. Liu, Z. Chang, L. Luo, et al., "Hierarchical $Zn_XCo_{3-x}O_4$ Nanoarrays with High Activity for Electrocatalytic Oxygen Evolution," *Chemistry of Materials* 26 (2014): 1889–1895, https://doi.org/10.1021/cm4040903.

19. G. Zhang, L. Zhao, G. Li, and L. Xu, "Thin Carbon Layer Covered Co_4N Cubes Encapsulated in N-Doped Porous Carbon Nanocage as Tri-Functional Catalysts with Enhanced Charge-Transfer Efficiency for Zn-Air Battery and Overall Water-Splitting," *Journal of Materials Chemistry A* 11 (2023): 11712–11720, https://doi.org/10.1039/D3TA01509B.

20. G. Zhu, H. Yang, Y. Jiang, et al., "Modulating the Electronic Structure of FeCo Nanoparticles in N-Doped Mesoporous Carbon for Efficient Oxygen Reduction Reaction," *Advanced Science* 9 (2022): 2200394, https://doi.org/10.1002/advs.202200394.

21. Q. Xu, H. Jiang, Y. Li, D. Liang, Y. Hu, and C. Li, "In-Situ Enriching Active Sites on Co-Doped Fe-Co_4N@N-C Nanosheet Array as Air Cathode for Flexible Rechargeable Zn-Air Batteries," *Applied Catalysis B: Environment and Energy* 256 (2019): 117893, https://doi.org/10.1016/j.apcatb.2019.117893.

22. C. Guan, A. Sumboja, W. Zang, et al., "Decorating Co/Conx Nanoparticles in Nitrogen-Doped Carbon Nanoarrays for Flexible and Rechargeable Zinc-Air Batteries," *Energy Storage Materials* 16 (2019): 243–250, https://doi.org/10.1016/j.ensm.2018.06.001.

23. T. I. Singh, A. Maibam, D. C. Cha, et al., "High-Alkaline Water-Splitting Activity of Mesoporous 3D Heterostructures: An Amorphous-Shell@Crystalline-Core Nano-Assembly of Co-Ni-Phosphate Ultrathin-Nanosheets and V- Doped Cobalt-Nitride Nanowires," *Advanced Science* 9 (2022): 2201311, https://doi.org/10.1002/advs.202201311.

24. Y. Sun, K. Mao, Q. Shen, et al., "Surface Electronic Structure Modulation of Cobalt Nitride Nanowire Arrays via Selenium Deposition for Efficient Hydrogen Evolution," *Advanced Functional Materials* 32 (2022): 2109792, https://doi.org/10.1002/adfm.202109792.

25. M. D. Meganathan, S. Mao, T. Huang, and G. Sun, "Reduced Graphene Oxide Intercalated Co_2C or Co_4N Nanoparticles as an Efficient and Durable Fuel Cell Catalyst for Oxygen Reduction," *Journal of Materials Chemistry A* 5 (2017): 2972–2980, https://doi.org/10.1039/C6TA09729D.

26. T. Liu, S. Zhao, Y. Wang, et al., "In Situ Anchoring Co–N–C Nanoparticles on Co_4N Nanosheets Toward Ultrastable Flexible Self-Supported Bifunctional Oxygen Electrocatalyst Enables Recyclable Zn–Air Batteries over 10 000 Cycles and Fast Charging," *Small* 18 (2022): 2105887, https://doi.org/10.1002/smll.202105887.

27. B. Liu, J. Cheng, H.-Q. Peng, et al., "In Situ Nitridated Porous Nanosheet Networked Co_3O_4–Co_4 N Heteronanostructures Supported on Hydrophilic Carbon Cloth for Highly Efficient Electrochemical Hydrogen Evolution," *Journal of Materials Chemistry A* 7 (2019): 775–782, https://doi.org/10.1039/C8TA09800J.

28. T. Sun, Q. Wu, R. Che, et al., "Alloyed Co–Mo Nitride as High-Performance Electrocatalyst for Oxygen Reduction in Acidic Medium," *ACS Catalysis* 5 (2015): 1857–1862, https://doi.org/10.1021/cs502029h.

29. K. Ito, K. Harada, K. Toko, H. Akinaga, and T. Suemasu, "Epitaxial Growth and Magnetic Characterization of Ferromagnetic Co_4N Thin Films on $Srtio_3$(001) Substrates by Molecular Beam Epitaxy," *Journal of Crystal Growth* 336 (2011): 40–43, https://doi.org/10.1016/j.jcrysgro.2011.09.038.

30. B. Cao, G. M. Veith, J. C. Neuefeind, R. R. Adzic, and P. G. Khalifah, "Mixed Close-Packed Cobalt Molybdenum Nitrides as Non-Noble Metal Electrocatalysts for the Hydrogen Evolution Reaction," *Journal of the American Chemical Society* 135 (2013): 19186–19192, https://doi.org/10.1021/ja4081056.

31. C. Zhang, N. Huang, Z. Zhai, et al., "Bifunctional Oxygen Electrocatalyst of Co_4N and Nitrogen-Doped Carbon Nanowalls/Diamond for High-Performance Flexible Zinc–Air Batteries," *Advanced Energy Materials* 13 (2023): 2301749, https://doi.org/10.1002/aenm.202301749.

32. X. F. Lu, S. L. Zhang, W. L. Sim, S. Gao, and X. W. Lou, "Phosphorized $CoNi_2S_4$ Yolk-Shell Spheres for Highly Efficient Hydrogen Production via Water and Urea Electrolysis," *Angewandte Chemie International Edition* 60 (2021): 22885–22891, https://doi.org/10.1002/anie.202108563.

33. Y. Cheng, Y. Tan, A. Li, Y. Zhang, and C. Cheng, "Spatially Decoupled Co Nanoparticles and Atomic Co-N_4 Sites with Exceptional Bifunctional Activity for High-Power and Durable Zn-Air Batteries," *Journal of Energy Chemistry* 116 (2026): 47–57, https://doi.org/10.1016/j.jechem.2025.12.055.

34. Z. Xu, M. Liu, S. Zhang, J. Zou, and B. Jiang, "Encapsulation of Alloy Heterojunctions in N/P-Doped Carbon Nano-Armor for Ultra-Long-Life Rechargeable/Flexible Zinc-Air Batteries," *Journal of Power Sources* 647 (2025): 237299, https://doi.org/10.1016/j.jpowsour.2025.237299.

35. D.-R. Deng, F. Xue, Y.-J. Jia, et al., "Co_4N Nanosheet Assembled Mesoporous Sphere as a Matrix for Ultrahigh Sulfur Content Lithium–Sulfur Batteries," *ACS Nano* 11 (2017): 6031–6039, https://doi.org/10.1021/acsnano.7b01945.

36. H. Liu, J. Lei, S. Yang, et al., "Boosting the Oxygen Evolution Activity over Cobalt Nitride Nanosheets through Optimizing the Electronic Configuration," *Applied Catalysis B: Environmental* 286 (2021): 119894, https://doi.org/10.1016/j.apcatb.2021.119894.

37. Z. Chen, Y. Song, J. Cai, et al., "Tailoring the D-Band Centers Enables Co_4N Nanosheets To Be Highly Active for Hydrogen Evolution Catalysis," *Angewandte Chemie International Edition* 57 (2018): 5076–5080, https://doi.org/10.1002/anie.201801834.

38. Q. Shi, Q. Liu, Y. Ma, et al., "High-Performance Trifunctional Electrocatalysts Based on FeCo/Co_2P Hybrid Nanoparticles for Zinc–Air Battery and Self-Powered Overall Water Splitting," *Advanced Energy Materials* 10 (2020): 1903854, https://doi.org/10.1002/aenm.201903854.

39. M. Perumalsamy, Y. Yoon, V. Elumalai, et al., "Engineering Spin State Modulation through Phosphorus-Coordinated Fe-NC Catalysts for Enhanced ORR Performance in Flexible Al-Air Batteries," *Applied Catalysis B: Environment and Energy* 372 (2025): 125329, https://doi.org/10.1016/j.apcatb.2025.125329.

40. J. Balamurugan, P. M. Austeria, J. B. Kim, et al., "Electrocatalysts for Zinc–Air Batteries Featuring Single Molybdenum Atoms in a Nitrogen-Doped Carbon Framework," *Advanced Materials* 35 (2023): 2302625, https://doi.org/10.1002/adma.202302625.

41. Y.-T. Deng, W.-T. Zhao, J.-J. Feng, L. Zhang, F. Yang, and A.-J. Wang, "High-Entropy Intermetallic/N-Doped Carbon Nanocages with Abundant Fine Carbon Nanotubes for Greatly Enhancing Oxygen Reduction in Zinc-Air Battery," *Journal of Energy Storage* 141 (2026): 119432, https://doi.org/10.1016/j.est.2025.119432.

42. C.-Y. Wang, C.-Z. Ren, K.-M. Fang, et al., "Synergistic Catalysis of Satellite Single-Atomic Fe Sites and RuFe Nanoclusters on N-Rich Carbon Nanoflowers for Boosting Oxygen Reduction," *Journal of Colloid and Interface Science* 699 (2025): 138169, https://doi.org/10.1016/j.jcis.2025.138169.

43. Q. Xu, H. Jiang, Y. Li, D. Liang, Y. Hu, and C. Li, "In-Situ Enriching Active Sites on co-Doped Fe-Co_4N@N-C Nanosheet Array as Air Cathode for Flexible Rechargeable Zn-Air Batteries," *Applied Catalysis B: Environment and Energy* 256 (2019): 117893, https://doi.org/10.1016/j.apcatb.2019.117893.

44. Y. Qin, M. Yang, C. Deng, W. Shen, R. He, and M. Li, "Theoretical Insight into Single Rh Atoms Anchored on N-Doped γ-Graphyne as an Excellent Bifunctional Electrocatalyst for the OER and ORR: Electronic Regulation of Graphitic Nitrogen," *Nanoscale* 13 (2021): 5800–5808, https://doi.org/10.1039/D0NR07513B.

45. L. Chai, J. Song, N. Jiang, et al., "An Isolated Dual Atomic Catalyst with over-Boiling Point Associated Strategy to Construct Superb Performance Rechargeable Zinc-Air Batteries," *Advanced Functional Materials* 35 (2025): 2504059, https://doi.org/10.1002/adfm.202504059.

46. Y. Li, J. Li, J. Huang, et al., "Boosting Electroreduction Kinetics of Nitrogen to Ammonia via Tuning Electron Distribution of Single-

Atomic Iron Sites," *Angewandte Chemie International Edition* 60 (2021): 9078–9085, https://doi.org/10.1002/anie.202100526.

47. Z. Wang, X. Jin, R. Xu, et al., "Cooperation between Dual Metal Atoms and Nanoclusters Enhances Activity and Stability for Oxygen Reduction and Evolution," *ACS Nano* 17 (2023): 8622–8633, https://doi.org/10.1021/acsnano.3c01287.

48. H. Li, R. Zeng, X. Feng, et al., "Oxidative Stability Matters: A Case Study of Palladium Hydride Nanosheets for Alkaline Fuel Cells," *Journal of the American Chemical Society* 144 (2022): 8106–8114, https://doi.org/10.1021/jacs.2c00518.

49. L. Wang, Z. Zeng, W. Gao, et al., "Tunable Intrinsic Strain in Two-Dimensional Transition Metal Electrocatalysts," *Science* 363 (2019): 870–874, https://doi.org/10.1126/science.aat8051.

50. J. Liu, D. Wang, K. Huang, et al., "Iodine-Doping-Induced Electronic Structure Tuning of Atomic Cobalt for Enhanced Hydrogen Evolution Electrocatalysis," *ACS Nano* 15 (2021): 18125–18134, https://doi.org/10.1021/acsnano.1c06796.

51. A. Kerschbaumer, D. Wielend, E. Leeb, et al., "How to Use a Rotating Ring-Disc Electrode (RRDE) Subtraction Method to Investigate the Electrocatalytic Oxygen Reduction Reaction?," *Catalysis Science & Technology* 13 (2023): 834–843, https://doi.org/10.1039/D2CY01744J.

52. Y. Wang, T. N. Pham, H. H. Halim, L. Yan, and Y. Morikawa, "DFT Investigation of the Oxygen Reduction Reaction over Nitrogen (N) Doped Graphdiyne as an Electrocatalyst: the Importance of Pre-Adsorbed OH* and the Solvation Effect," *Materials Advances* 4 (2023): 6542–6552, https://doi.org/10.1039/D3MA00502J.

53. A. A. Emery and C. Wolverton, "High-Throughput DFT Calculations of Formation Energy, Stability and Oxygen Vacancy Formation Energy of ABO_3 Perovskites," *Scientific Data* 4 (2017): 170153, https://doi.org/10.1038/sdata.2017.153.

54. E. E. Siddharthan, S. Ghosh, and R. Thapa, "Site Specific Descriptors for Oxygen Evolution Reaction Activity on Single Atom Catalysts Using QMML," *Journal of Materials Chemistry A* 12 (2024): 19176–19186, https://doi.org/10.1039/D4TA02610A.

55. G. Deng, H. Yun, Y. Chen, et al., "Ferrocene-Functionalized Atomically Precise Metal Clusters Exhibit Synergistically Enhanced Performance for CO_2 Electroreduction," *Angewandte Chemie International Edition* 64 (2025): 202418264, https://doi.org/10.1002/anie.202418264.

56. S. Bhardwaj, A. Pathak, S. K. Das, P. Das, R. Thapa, and R. S. Dey, "Decoding Dual-Functionality in N-Doped Defective Carbon: Unveiling Active Sites for Bifunctional Oxygen Electrocatalysis," *Small* 21 (2025): 2411035, https://doi.org/10.1002/smll.202411035.

57. X. Yang, H. Mao, Z. Zhou, et al., "Biphasic Nanoalloys-Based Trifunctional Monolith for High-Performance Flexible Zn-Air Batteries and Self-Driven Water Splitting," *Advanced Functional Materials* 34 (2024): 2402933, https://doi.org/10.1002/adfm.202402933.

58. B. Hammer and J. K. Nørskov, "Theoretical Surface Science and Catalysis-Calculations and Concepts," *Advances in Catalysis* 45 (2000): 71–129, https://doi.org/10.1016/S0360-0564(02)45013-4.

59. S. Paul, A. Adalder, N. Barman, et al., "Boosting Selective Nitrogen Oxidation to Nitric Acid by Synergizing Cobalt Phthalocyanine on Carbon Nitride Surface," *Advanced Functional Materials* 34 (2024): 2408314, https://doi.org/10.1002/adfm.202408314.

60. X. Zhong, Z. Zheng, J. Xu, et al., "Flexible Zinc–Air Batteries with Ampere-Hour Capacities and Wide-Temperature Adaptabilities," *Advanced Materials* 35 (2023): 2209980, https://doi.org/10.1002/adma.202209980.

61. X. Wang, B. Wang, P. Lei, et al., "Polycation-Regulated Hydrogel Electrolytes with Nanoscale Hydrophobic Confinement Inducing Zn(002) Deposition for Highly Reversible Zinc Anodes," *Energy & Environmental Science* 17 (2024): 6640–6655, https://doi.org/10.1039/D4EE01660B.

62. J. Cao, D. Zhang, C. Gu, et al., "Manipulating Crystallographic Orientation of Zinc Deposition for Dendrite-Free Zinc Ion Batteries," *Advanced Energy Materials* 11 (2021): 2101299, https://doi.org/10.1002/aenm.202101299.

63. A. M. Paswan, V. S. Thakur, S. Banerjee, and C. R. Raj, "Electrochemical Engineering of Anode with Zincophilic Polymer Interface for Reversible Zinc Battery," *Advanced Functional Materials* 35 (2025): 2412370, https://doi.org/10.1002/adfm.202412370.

64. X. Fan, R. Zhang, S. Sui, et al., "Starch-Based Superabsorbent Hydrogel with High Electrolyte Retention Capability and Synergistic Interface Engineering for Long-Lifespan Flexible Zinc−Air Batteries," *Angewandte Chemie International Edition* 62 (2023): 202302640, https://doi.org/10.1002/anie.202302640.

65. H. Li, F. Xu, Y. Li, and J. Sun, "Self-Healing Ionogel-Enabled Self-Healing and Wide-Temperature Flexible Zinc-Air Batteries with Ultra-Long Cycling Lives," *Advanced Science* 11 (2024): 2402193, https://doi.org/10.1002/advs.202402193.

66. M. Jiao, L. Dai, H.-R. Ren, et al., "A Polarized Gel Electrolyte for Wide-Temperature Flexible Zinc-Air Batteries," *Angewandte Chemie International Edition* 135 (2023): 202301114, https://doi.org/10.1002/ange.202301114.

67. Z. Lu, Q. Yang, H. Pan, et al., "Bifunctional Oxygen Electrocatalysis at Co-B,N,S-Graphene Composite Investigated by Scanning Electrochemical Microscopy at Variable Temperatures and Its Application in Zn-Air Battery," *Electrochimica Acta* 389 (2021): 138751, https://doi.org/10.1016/j.electacta.2021.138751.

Supporting Information

Additional supporting information can be found online in the Supporting Information section.

Supporting File 1: aenm70906-sup-0001-SuppMat.pdf.

Supporting File 2: aenm70906-sup-0002-VideoS13mp4.

Supporting File 3: aenm70906-sup-0003-VideoS2.mp4.

Supporting File 4: aenm70906-sup-0004-VideoS3.mp4.

Supporting File 5: aenm70906-sup-0005-VideoS4.mp4.